

# CORE-COLLAPSE VERY MASSIVE STARS: EVOLUTION, EXPLOSION, AND NUCLEOSYNTHESIS OF POPULATION III 500–1000 $M_{\odot}$ STARS

TAKUYA OHKUBO,<sup>1</sup> HIDEYUKI UMEDA,<sup>1</sup> KEIICHI MAEDA,<sup>2</sup> KEN’ICHI NOMOTO,<sup>1,3</sup>  
 TOMOHARU SUZUKI,<sup>1</sup> SACHIKO TSURUTA,<sup>4</sup> AND MARTIN J. REES<sup>5</sup>

*Received 2005 May 21; accepted 2006 March 20*

## ABSTRACT

We calculate evolution, collapse, explosion, and nucleosynthesis of Population III very massive stars with 500 and 1000  $M_{\odot}$ . Presupernova evolution is calculated in spherical symmetry. Collapse and explosion are calculated by a two-dimensional code, based on the bipolar jet models. We compare the results of nucleosynthesis with the abundance patterns of intracluster matter, hot gases in M82, and extremely metal-poor stars in the Galactic halo. It was found that both 500 and 1000  $M_{\odot}$  models enter the region of pair instability but continue to undergo core collapse. In the presupernova stage, silicon-burning regions occupy a large fraction, more than 20% of the total mass. For moderately aspherical explosions, the patterns of nucleosynthesis match the observational data of both the intracluster medium and M82. Our results suggest that explosions of Population III core-collapse very massive stars contribute significantly to the chemical evolution of gases in clusters of galaxies. For Galactic halo stars our [O/Fe] ratios are smaller than the observational abundances. However, our proposed scenario is naturally consistent with this outcome. The final black hole masses are  $\sim 230$  and  $\sim 500 M_{\odot}$  for the 500 and 1000  $M_{\odot}$  models, respectively. This result may support the view that Population III very massive stars are responsible for the origin of intermediate-mass black holes, which were recently reported to be discovered.

*Subject heading:* nuclear reactions, nucleosynthesis, abundances — stars: abundances — stars: evolution

## 1. INTRODUCTION

One of the most interesting challenges in astronomy is the investigation of the mass and properties of first-generation “Population III” (Pop III) stars and how various elements have been synthesized in the early universe. Just after the big bang these elements were mostly only H, He, and a small amount of light elements (Li, Be, B, etc.). Heavier elements, such as C, O, Ne, Mg, Si, and Fe, were synthesized during the evolution of later generation stars, and massive stars exploded as supernovae (SNe), releasing heavy elements into space.

Stars end their lives differently depending on their initial masses  $M$ . Here the Pop III stars are assumed to undergo too little mass loss to affect the later core evolution. Therefore, the fates of Pop III stars are summarized as follows. Those stars lighter than 8  $M_{\odot}$  form white dwarfs. Those with 8–130  $M_{\odot}$  undergo ONe-Fe core collapse at a last stage of their evolution, leaving neutron stars or black holes. Some of these stars explode, creating core-collapse supernovae. Stars with 130–300  $M_{\odot}$  undergo electron-positron pair creation instability during oxygen burning, releasing more energy by nuclear burning than the gravitational binding energy of the whole star, and hence these stars disrupt completely, forming pair-instability supernovae (PISNe). Stars with 300–10<sup>5</sup>  $M_{\odot}$  also enter into the pair-instability region, but

continue to collapse. Fryer et al. (2001) calculated the evolution of 260 and 300  $M_{\odot}$  stars and obtained the result that a 260  $M_{\odot}$  star ends up as a PISN and a 300  $M_{\odot}$  star collapsed. Stars over  $\sim 10^5 M_{\odot}$  collapse, owing to general relativistic instability, before reaching the main sequence. The core-collapse SNe (Type II, Ib, and Ic SNe) release mainly  $\alpha$ -elements such as O, Mg, Si, and Ca and some Fe-peak elements as well.

It has been suggested that the initial mass function (IMF) of first-generation Pop III stars may be different from the present function, i.e., more massive stars existed in the early universe (e.g., Nakamura & Umemura 1999; Abel et al. 2000; Bromm et al. 2002; Omukai & Palla 2003). Some authors (e.g., Wasserburg & Qian 2000; Qian et al. 2002; Qian & Wasserburg 2002; and Yoshida et al. 2004) argued that existence of very massive stars (VMSs) in the early universe is consistent with abundance data of Ly $\alpha$  systems. Numerical simulations by, e.g., Bromm & Loeb (2004) indicate that the maximum mass of Pop III stars that will form is  $\sim 300$ –500  $M_{\odot}$ . Omukai & Palla (2003), however, point out that under certain conditions, VMSs much heavier than 300  $M_{\odot}$  can be formed in the zero-metallicity environment. Tan & McKee (2004) calculated star formation by taking rotation and disk structure and concluded that first-generation stars should be much more massive than 30  $M_{\odot}$ . Another scenario for the formation of VMSs for any metallicity has been presented by Ebisuzaki et al. (2001), Portegies Zwart et al. (1999, 2004), and Portegies Zwart (2006), where VMSs are formed by merging of less massive stars in the environment of very dense star clusters.

In the present paper we call the stars with  $M \gtrsim 10^5 M_{\odot}$  “super-massive stars” (SMSs), and the stars with  $M = 130$ –10<sup>5</sup>  $M_{\odot}$  “very massive stars” (VMSs). Among VMSs we define  $M > 300 M_{\odot}$  stars as “core-collapse very massive stars” (CVMSs), in order to clarify the distinction between the PISN mass range and the core-collapse range. Here we focus on CVMSs and deal with 500 and 1000  $M_{\odot}$  models.

Such CVMSs might have released a large amount of heavy elements into space by mass loss and/or supernova explosions,

<sup>1</sup> Department of Astronomy, School of Science, University of Tokyo, 7-3-1 Hongo, Bunkyo-ku, Tokyo 113-0033, Japan; ohkubo@astron.s.u-tokyo.ac.jp, umeda@astron.s.u-tokyo.ac.jp, nomoto@astron.s.u-tokyo.ac.jp, suzuki@astron.s.u-tokyo.ac.jp.

<sup>2</sup> Department of Earth Science and Astronomy, Graduate School of Arts and Sciences, University of Tokyo, 3-8-1, Komaba, Meguro-ku, Tokyo 153-8902, Japan; maeda@esa.c.u-tokyo.ac.jp.

<sup>3</sup> Research Center for the Early Universe, School of Science, University of Tokyo, 7-3-1 Hongo, Bunkyo-ku, Tokyo 113-0033, Japan.

<sup>4</sup> Department of Physics, Montana State University, Bozeman, MT 59717-3840; uphst@gemini.msu.montana.edu.

<sup>5</sup> Institute of Astronomy, Cambridge University, Madingley Road, Cambridge CB3 0HA, UK; mjr@ast.cam.ac.uk.

and they might have significantly contributed to the early galactic chemical evolution, if they were the source of reionization of intergalactic H and He (e.g., Gnedin & Ostriker 1997; Venkatesan et al. 2003). The reionization of intergalactic He has traditionally been attributed to quasars. However, according to the results of the *Wilkinson Microwave Anisotropy Probe* (*WMAP*) observation in 2003, reionization in the universe took place as early as 0.2–0.3 billion years after the big bang (redshift  $z \gtrsim 20$ ; Kogut et al. 2003). Therefore, these Pop III CVMSs might provide a better alternative channel that could operate at redshifts higher than what is assumed for quasars (Bromm et al. 2001).

The question of whether CVMSs ( $\sim 300\text{--}10^5 M_\odot$ ) actually existed is of great importance, for instance, in understanding the origin of intermediate-mass black holes (IMBHs;  $\sim 5 \times (10^2\text{--}10^4) M_\odot$ ). Stellar-mass black holes ( $\sim 10 M_\odot$ ) are formed as the central compact remnants of ordinary massive ( $25\text{--}130 M_\odot$ ) stars at the end of their evolution, while supermassive black holes (SMBHs;  $\sim 10^5\text{--}10^9 M_\odot$ ) are now known to exist in the center of almost all galaxies (e.g., Kormendy & Richstone 1995; Bender 2005). IMBHs have not been found until recently. However, there is a strong possibility that some IMBHs have indeed been found (e.g., Barth et al. 2005 for most recent review). Matsumoto et al. (2001) reported possible identification of a  $\gtrsim 700 M_\odot$  black hole in M82 by using *Chandra* data. As to the formation of SMBHs, there are several scenarios (e.g., Rees 2002, 2003). SMBHs may be formed directly from supermassive halos of dark matter (e.g., Marchant & Shapiro 1980; Bromm & Loeb 2003). Ebisuzaki et al. (2001) suggested a scenario in which IMBHs grow to a SMBH by merging and swallowing of many of these objects. If CVMSs actually existed, they could be considered as natural progenitors of IMBHs.

Motivated by these backgrounds, here we calculate the evolution, collapse, explosion, and nucleosynthesis of Pop III CVMSs (over  $300 M_\odot$ ). These stars are expected to form black holes directly at the end of evolution. It has not been known yet if they will explode as SNe. However, if the star is rotating, the whole star will not become a black hole at once, but it is expected to form an accretion disk around the central remnant (e.g., Shibata & Shapiro 2002). After forming an accretion disk, jetlike explosions may occur by extracting energy from the accretion disk and/or the black hole itself (Fryer et al. 2001; MacFadyen et al. 2001; Maeda & Nomoto 2003). Therefore, in our current explosion and collapse calculations, we adopt a two-dimensional approach including accretion along the equatorial direction and jets toward the polar direction.

We compare our results of nucleosynthesis with the observed abundance data of intracluster medium (ICM), intergalactic medium (IGM), gases in the central part of M82, and extremely metal-poor (EMP) stars in the Galactic halo. Since it is very difficult to observe directly the explosions of the first-generation stars due to the large distance (redshift  $z \gtrsim 20$ ), currently comparison of the kind carried out in this study will offer a powerful method to support the existence of such very massive stars.

After describing the basic methods adopted and the assumptions made for our models in § 2, the results are presented and discussed in § 3, and they are compared with observations in § 4. Further discussion and concluding remarks are given in § 5.

## 2. METHODS, ASSUMPTIONS, AND MODELS

We calculate evolution, core collapse, explosion, and nucleosynthesis of very massive stars with 500 and  $1000 M_\odot$ . As mentioned in § 1, such massive stars may be formed in a metal-free environment. We start our evolutionary calculations by assum-

ing that the stars have 500 and  $1000 M_\odot$  with zero metallicity on the pre-main sequence. As our starting approximation we neglect radiative mass loss due to zero metallicity (Kudritzki 2000). Ibrahim et al. (1981), Baraffe et al. (2001), and Nomoto et al. (2003) showed that pulsational mass loss is not so effective for metal-free stars, so we also neglect the pulsational mass loss. To calculate presupernova evolution, we adopt the stellar evolution code constructed by Umeda & Nomoto (2002) based on the Henyey method. This code is developed from the codes constructed by Nomoto & Hashimoto (1988) and Umeda et al. (2000). The nuclear reaction network for calculating nucleosynthesis and energy generation at each stage of the evolution is developed by Hix & Thielemann (1996). We include 51 isotopes up to Si until He burning ends, and 240 up to Ge afterward. Our evolutionary calculations are carried out from the pre-main sequence up to the iron-core collapse, where the central density reaches as high as  $2 \times 10^{10} \text{ g cm}^{-3}$ . When the temperature reaches  $5 \times 10^9 \text{ K}$ , where “nuclear statistical equilibrium” (hereafter NSE) is realized, the abundance of each isotope is determined for a given set of density, temperature, and  $Y_e$ . Here  $Y_e$  is the number of electrons per nucleon, defined as

$$Y_e = \sum_i \frac{Z_i}{A_i} X_i, \quad (1)$$

where  $Z_i$  is the atomic number,  $A_i$  is the mass number, and  $X_i$  is the mass fraction of species  $i$ .  $Y_e$ , as well as density and temperature, is a key quantity in determining the abundance of each element. We assume NSE at  $\log T(\text{K}) \geq 9.7$ .

The explosion mechanism of core-collapse supernovae is not well understood. Moreover, we do not know beforehand how very massive stars over  $300 M_\odot$  explode due to strong gravitation even when they are rotating. In this study, therefore, instead of going into the problem of whether such massive stars actually explode, we investigate the conditions required for these stars to explode by exploring several situations with various models. For the explosion in the hydrodynamical simulation, we adopt the two-dimensional (2D) Newtonian hydrodynamical code constructed by Maeda & Nomoto (2003) and Maeda (2004). This code adopts the Eulerian coordinate and solves Euler equations based on Roe’s scheme (Hachisu et al. 1992, 1994). Previously, 2D simulations of jet-induced supernova explosions have been carried out by many authors for ordinary massive stars with  $\sim 25\text{--}40 M_\odot$  (Khokhlov et al. 1999; MacFadyen et al. 2001; Nagataki 2000; Maeda et al. 2002, 2006; Maeda & Nomoto 2003). However, there have been no such detailed calculations for CVMSs with  $M \gtrsim 500 M_\odot$ . Because temperatures are so high at the explosion, the pressure is radiation-dominated, and hence we use the equation of state for the radiation and electron-positron pairs with the adiabatic index of 4/3.

The explosion models to be explored are summarized in Tables 1 and 2. Jets, which are supposed to be injected from the accretion disk, are considered to be the energy source of the explosion. We first choose the initial black hole mass, and the outer matter accretes toward the central object. Because our hydrodynamical code includes gravitational force, the final black hole mass and the ejected mass are determined as the results of the calculations for a set of given parameters (Maeda & Nomoto 2003). One of the purposes of this study is to explore the conditions necessary for the stars to explode when jets are injected. As typical cases we choose the initial black hole mass,  $M_{\text{BH0}}$ , at  $100 M_\odot$  for the  $1000 M_\odot$  star and  $50 M_\odot$  for the  $500 M_\odot$  star. However, in order to investigate the dependence of results on

TABLE 1  
THE HIGHER RESOLUTION MODELS

| Models<br>(1) | Progenitor<br>( $M_{\odot}$ )<br>(2) | $M_{\text{BH0}}$<br>( $M_{\odot}$ )<br>(3) | $R_0$<br>(km)<br>(4) | $\theta_{\text{jet}}$<br>(deg)<br>(5) | $\epsilon$<br>(6) | $\mu$<br>(7) | $F_{\text{thrm}}$<br>(8) | $v_{\text{jet}}/c$<br>(9) |
|---------------|--------------------------------------|--|----------------------|---------------------------------------|-------------------|--------------|--------------------------|---------------------------|
| A-1 .....     | 1000                                 | 100  | $1.5 \times 10^4$    | 15                                    | 0.01              | 0.1          | 0.01                     | 0.45                      |
| A-2 .....     | 1000                                 | 100  | $1.5 \times 10^4$    | 30                                    | 0.01              | 0.1          | 0.01                     | 0.45                      |
| B-1 .....     | 1000                                 | 100  | $1.5 \times 10^4$    | 15                                    | 0.01              | 0.005        | 0.95                     | 0.45                      |
| B-2 .....     | 1000                                 | 100  | $1.5 \times 10^4$    | 15                                    | 0.005             | 0.0025       | 0.95                     | 0.45                      |
| B-3 .....     | 500                                  | 50   | $1.1 \times 10^4$    | 15                                    | 0.01              | 0.005        | 0.95                     | 0.45                      |

NOTES.—Col. (3): Initial black hole mass  $M_{\text{BH0}}$ . Col. (4): The radius at the inner boundary of the simulations  $R_0$ . Col. (5): Jet injected angle  $\theta_{\text{jet}}$ . Col. (6): Energy transformation efficiency  $\epsilon$ . Col. (7): The mass fraction in which accreted matter is ejected as jet  $\mu$ . Col. (9): The jet velocity normalized by the speed of light  $v_{\text{jet}}$ .

this parameter, we also explore larger and smaller values of  $M_{\text{BH0}}$ .

We adopt the spherical polar coordinate with the number of meshes set to  $150 \times 60$  for five models (higher resolution; A-1, A-2, B-1, B-2, and B-3), and  $100 \times 30$  for the rest (lower resolution). The latter models are chosen so that we can search for parameter dependence quickly. We describe our results mainly based on those of higher resolution models. However, we include lower resolution models to explore the detailed dependence on parameters. We also calculate model B-2 with lower resolution in order to numerically compare the two resolutions. The difference of the quantities we give in Tables 3, 4, 6, and 7 between the two resolutions is around 10%.

At the beginning of hydrodynamical simulations, the region  $M_{\text{BH0}} < M_r$  is mapped onto the computational domain. The central part ( $M_r \leq M_{\text{BH0}}$ ) is displaced by a point mass. The inner boundary of the simulations is set at the radius  $R_0$  (see Tables 1 and 2). In the computational domain, we assume that the effect of rotation is negligible. This assumption applies if the specific angular momentum  $j_{17} = j/10^{17} \text{ cm}^2 \text{ s}^{-1}$  in the progenitor star is in the range  $6.3 \leq j_{17} \ll 45$ , where the lower and upper limits correspond to the conditions that the disk forms beyond the Schwarzschild radius and well below the inner boundary of our computational domain. If  $j_{17} \sim 6.3$ , which is favorable in order to make an efficiently accreting disk (Narayan et al. 2001), then the rotational force is at most a few percent of the gravitational force at the inner boundary.

For the jet injection, we choose various values for the parameter,  $\theta_{\text{jet}}$ , the angle from the polar axis. The jet is injected into the direction of  $0 \leq \theta \leq \theta_{\text{jet}}$ . At the direction  $\theta > \theta_{\text{jet}}$ , the inner boundary is treated as follows. It is set to be transmitted (absorbed; i.e., vanishing radial gradient of all variables) or reflected if the material just above the boundary has negative (accreting) or positive sign. These boundary conditions are used in previous stud-

ies on jet-induced supernova explosions (Khokhlov et al. 1999; MacFadyen et al. 2001; Maeda & Nomoto 2003). It should be noted that by using the transmitted boundary condition for the accretion case and neglecting pressure and rotational support below the boundary, we may overestimate the accretion rate.

The energy and mass injected by the jets per unit time are connected with the properties of accreting matter as (Maeda & Nomoto 2003)

$$\dot{E}_{\text{jet}} = \epsilon \dot{M}_{\text{acc}} c^2 = \dot{E}_{\text{thrm}} + \left( \frac{1}{2} \rho_{\text{jet}} v_{\text{jet}}^2 \right) v_{\text{jet}} A_{\text{jet}}, \quad (2)$$

$$\dot{M}_{\text{jet}} = \mu \dot{M}_{\text{acc}} = \rho_{\text{jet}} v_{\text{jet}} A_{\text{jet}}, \quad (3)$$

where  $\dot{M}_{\text{acc}}$  is the accretion rate,  $\dot{E}_{\text{jet}}$  is the injected energy per unit time,  $\dot{M}_{\text{jet}}$  is the mass spouted per unit time,  $\epsilon$  is the energy transformation efficiency,  $\mu$  is the mass fraction of the jets to the accreted matter,  $\rho_{\text{jet}}$  is the jet density,  $v_{\text{jet}}$  is the jet velocity, and  $A_{\text{jet}}$  is the area over which the jet is spouted. We treat  $\epsilon$  and  $\mu$  as free parameters to be varied to explore the explosion energy.

We consider two cases for the form of the injected energy. One is that almost all the energy of the jet is given as kinetic energy (case A). The other is that almost all the energy is given as thermal energy (case B). We introduce a parameter  $F_{\text{thrm}}$  defined as

$$F_{\text{thrm}} = \dot{E}_{\text{thrm}} / \dot{E}_{\text{jet}}, \quad (4)$$

i.e., the ratio of thermal energy in the jet to the total jet energy per unit time. This parameter is set to 0.01 for case A, and to 0.9 or 0.95 for case B. By using equations (2), (3), and (4), we obtain the jet velocity

$$v_{\text{jet}} = \left[ \frac{2\epsilon(1 - F_{\text{thrm}})}{\mu} \right]^{1/2} c. \quad (5)$$

TABLE 2  
THE LOWER RESOLUTION MODELS

| Models    | Progenitor<br>( $M_{\odot}$ ) | $M_{\text{BH0}}$<br>( $M_{\odot}$ ) | $R_0$<br>(km)     | $\theta_{\text{jet}}$<br>(deg) | $\epsilon$ | $\mu$  | $F_{\text{thrm}}$ | $v_{\text{jet}}/c$ |
|-----------|-------------------------------|-------------------------------------|-------------------|--------------------------------|------------|--------|-------------------|--------------------|
| A-3 ..... | 1000                          | 100                                 | $1.5 \times 10^4$ | 15                             | 0.005      | 0.05   | 0.01              | 0.45               |
| A-4 ..... | 1000                          | 100                                 | $1.5 \times 10^4$ | 15                             | 0.002      | 0.02   | 0.01              | 0.45               |
| A-5 ..... | 1000                          | 50                                  | $8.4 \times 10^3$ | 15                             | 0.005      | 0.05   | 0.01              | 0.45               |
| A-6 ..... | 1000                          | 200                                 | $2.7 \times 10^4$ | 15                             | 0.01       | 0.1    | 0.01              | 0.45               |
| A-7 ..... | 500                           | 50                                  | $8.4 \times 10^3$ | 15                             | 0.01       | 0.1    | 0.01              | 0.45               |
| B-2 ..... | 1000                          | 100                                 | $1.5 \times 10^4$ | 15                             | 0.005      | 0.0025 | 0.95              | 0.45               |
| B-4 ..... | 1000                          | 100                                 | $1.5 \times 10^4$ | 15                             | 0.01       | 0.02   | 0.9               | 0.32               |
| B-5 ..... | 1000                          | 100                                 | $1.5 \times 10^4$ | 15                             | 0.005      | 0.01   | 0.9               | 0.32               |

Equations (2), (3), and (4) give a complete set of jet properties at the inner boundary. In case A the jet carries most energy toward the polar (jet-injected) direction, and hence the model is highly nonspherical. For this case, we set the ratio between the two parameters,  $\epsilon/\mu$ , to 0.1. Because we perform a Newtonian calculation, the larger we set  $\epsilon$  the larger we need to set  $\mu$ , so that the jet material does not exceed or approach the speed of light. For case B on the other hand, because of the dominant thermal energy, the models become more spherical, because thermal motion is random and nondirectional. For this case, we set larger  $\epsilon$  values for the same  $\mu$  as compared with case A. This means that the jet is something like a hot bubble.

One of our primary purposes is to investigate how much heavy elements are synthesized and ejected by the explosion. Therefore, we stop the calculations when all of the following conditions are satisfied:

1.  $\dot{M}_{\text{acc}}$  decreases enough below  $0.1 M_{\odot} \text{ s}^{-1}$ , i.e.,  $\lesssim 0.02 M_{\odot} \text{ s}^{-1}$ .
2. Total explosion energy  $E_{\text{tot}}$  becomes much larger than the absolute gravitational binding energy  $|E_{\text{grav}}|$ ,  $E_{\text{tot}} \gtrsim 10|E_{\text{grav}}|$ . These criteria mean that accretion has almost stopped.
3. The maximum temperature of the matter decreases below  $8 \times 10^8 \text{ K}$ . This means that explosive nucleosynthesis no longer occurs at such low temperatures.

Under these criteria, calculations sometimes end before jets reach the stellar surface.

Maeda & Nomoto (2003) used helium stars (the hydrogen envelope is removed by mass loss) as the initial models and carried out the calculations for about 100 s until the jet reaches the stellar surface, and the expansion becomes homologous. In contrast the radii of the stars we use here are of the order  $10^2 R_{\odot}$  ( $\sim 10^{13} \text{ cm}$ ) because they have the hydrogen-rich envelope. Because we investigate the first-generation stars, the mass loss will not be effective due to the metal-free environment. Therefore, it is reasonable to examine a hydrogen-rich star rather than a He star.

We calculated explosive nucleosynthesis by using temporal histories of density and temperature stored during hydrodynamical calculations. The reaction network we use includes 280 isotopes up to  $^{79}\text{Br}$ . At high temperatures,  $T_9 = T/10^9 \text{ K} > 5$ , NSE is realized. We use the NSE code (Hix & Thielemann 1996) for  $T_9 > 6$ .

The jet matter should be included in the ejected matter, and we need to calculate its nucleosynthesis. We do not know which of the accreted matter is injected as jets, and so the final chemical composition is uncertain. However, Pruet et al. (2004) carried out nucleosynthesis of disk wind for various  $Y_e$  values. MacFadyen & Woosley (1999) and MacFadyen (2003) also considered disk wind. Based on these works in this study, we make the following assumptions:

1. Because the jet matter is injected through the inner region (from the accretion disk), it should have experienced high temperatures at which NSE is realized ( $T_9 > 5$ ).
2. The jet matter expands adiabatically after it is injected (i.e., entropy is conserved).
3. The accreted matter is mostly accreted while the accretion rate  $\dot{M}_{\text{acc}}$  is of the order  $10\text{--}10^2 M_{\odot} \text{ s}^{-1}$ . It is likely that  $\rho$  varies depending on when the jet material is injected. Therefore  $s$  (entropy density,  $\propto T^3/\rho$ ) is likely to vary as well.
4. For the value of  $Y_e$  we assume  $0.48 \leq Y_e \leq 0.52$ .

Based on these assumptions, we start the calculation of nucleosynthesis of the jet matter from  $T_9 = 6$ , using the historical

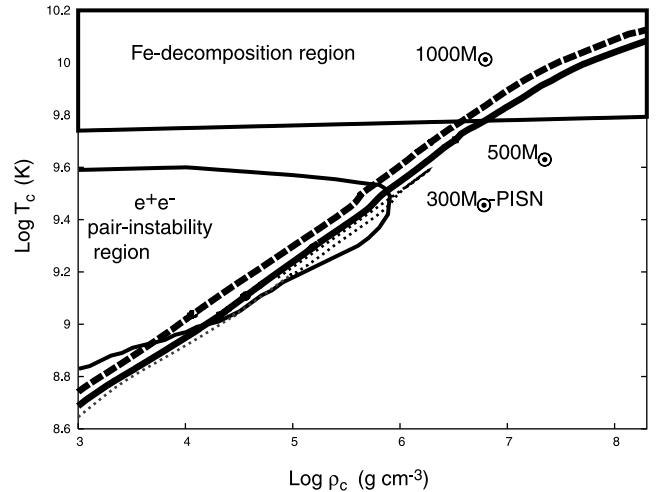


FIG. 1.—Evolutionary tracks of central temperature and density of the stars with  $300 M_{\odot}$  (thin dotted line),  $500 M_{\odot}$  (thick solid line), and  $1000 M_{\odot}$  (thick dashed line).

temperature and density data of the first test particle of the jet (injected at the first stage of the explosion) in model A-2 (history A) and the changed entropy data (double [history B] or triple [history C] the density at the same temperature). In other words we use three  $\rho$ - $T$  histories (history A:  $[\rho(t), T(t)]$ , history B:  $[2\rho(t), T(t)]$ , and history C:  $[3\rho(t), T(t)]$ ), where the set  $[\rho(t), T(t)]$  is given by the hydrodynamic simulations.  $Y_e$  is parameterized at 0.48, 0.49, 0.50, 0.51, and 0.52. We calculate 15 patterns and average these results to the first approximation.  $Y_e$  and entropy of the jet material can change when it is ejected. Therefore, here we consider the combination of jets with different values of these parameters. These assumptions still include large uncertainty, but our aim is just to roughly estimate the amount of  $^{56}\text{Ni}$ . The larger the mass of the jet, the larger we expect the uncertainties to be.

### 3. RESULTS

#### 3.1. Presupernova Evolution

##### 3.1.1. Evolutionary Tracks

Figure 1 shows the evolutionary tracks of the central density-temperature relation for 500 and  $1000 M_{\odot}$  stars. We also plot, for comparison, the track of a  $300 M_{\odot}$  star, which results in the pair-instability supernova. Generally, more massive stars have higher entropies (lower densities) at the same temperatures (i.e., at the same burning stage). Although each star passes through the region of electron-positron pair instability, both 500 and  $1000 M_{\odot}$  stars proceed to iron-core collapse (Fe-decomposition region in Fig. 1), unlike the  $300 M_{\odot}$  star. The 500 and  $1000 M_{\odot}$  stars do not become pair-instability supernovae, although they do pass through the pair-instability region because the energy released at this stage is less than the gravitational binding energy of the star (Rakavy et al. 1967; Bond et al. 1984; Glatzel et al. 1985; Woosley 1986).

##### 3.1.2. Presupernova Model

Figure 2 shows the presupernova chemical composition for the 500 and  $1000 M_{\odot}$  stars. In the region labeled “NSE region” NSE is realized. For this region we calculate the evolutionary changes in terms of  $(Y_e, \rho, T)$  to obtain the NSE abundances. One can see the onion-like structure from the center to the surface, i.e., the iron core, silicon layer, oxygen layer, helium layer, and

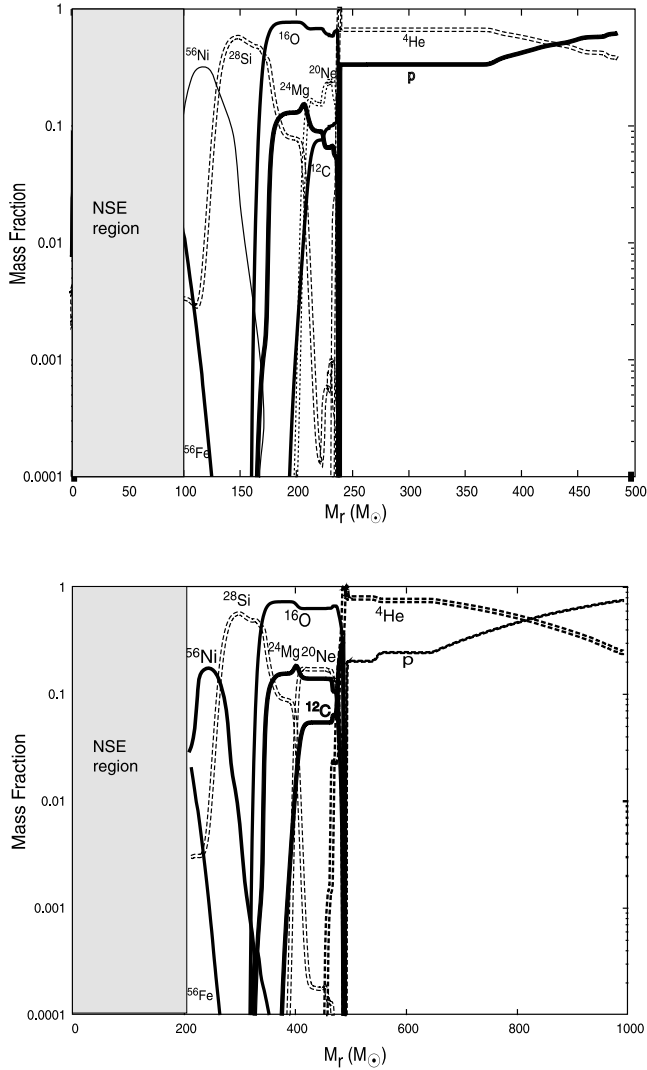


FIG. 2.—Chemical composition just before the explosion (when the central density reaches  $10^{10} \text{ g cm}^{-3}$ ) of the  $500 M_{\odot}$  star (top) and  $1000 M_{\odot}$  star (bottom). The iron core occupies more than 20% of the total mass for both cases.

hydrogen-rich layer. Here we define the iron core as the region where the mass fraction of Si is less than 10%. The iron core occupies up to  $130 M_{\odot}$  of mass from the center for the  $500 M_{\odot}$  star and  $250 M_{\odot}$  for the  $1000 M_{\odot}$  star. For both cases, they occupy a quarter of the total mass. This fraction is much larger than that in ordinary massive stars. For example, in a  $25 M_{\odot}$  star the iron core is about  $1.6 M_{\odot}$  (Umeda et al. 2000), less than 10% of the total mass, because of the difference of the density and temperature structure.

Figure 3 shows the density and temperature structure of the two stars just before the explosion (when the central density reaches  $10^{10} \text{ g cm}^{-3}$ ), which is compared with the  $25 M_{\odot}$  model. The density and temperature gradients for the 500 and  $1000 M_{\odot}$  stars are smaller than those of the  $25 M_{\odot}$  star, and hence the regions with high temperature and high density are larger. Then the fraction of the iron core is larger. The large drop of density at  $M_r/M_{\text{tot}} \sim 0.5$  for the 500 and  $1000 M_{\odot}$  stars in Figure 3 corresponds to the boundary between the oxygen and helium layer.

### 3.2. Explosion Hydrodynamics

We describe the results of explosion hydrodynamics in this subsection and nucleosynthesis in the next subsection, show-

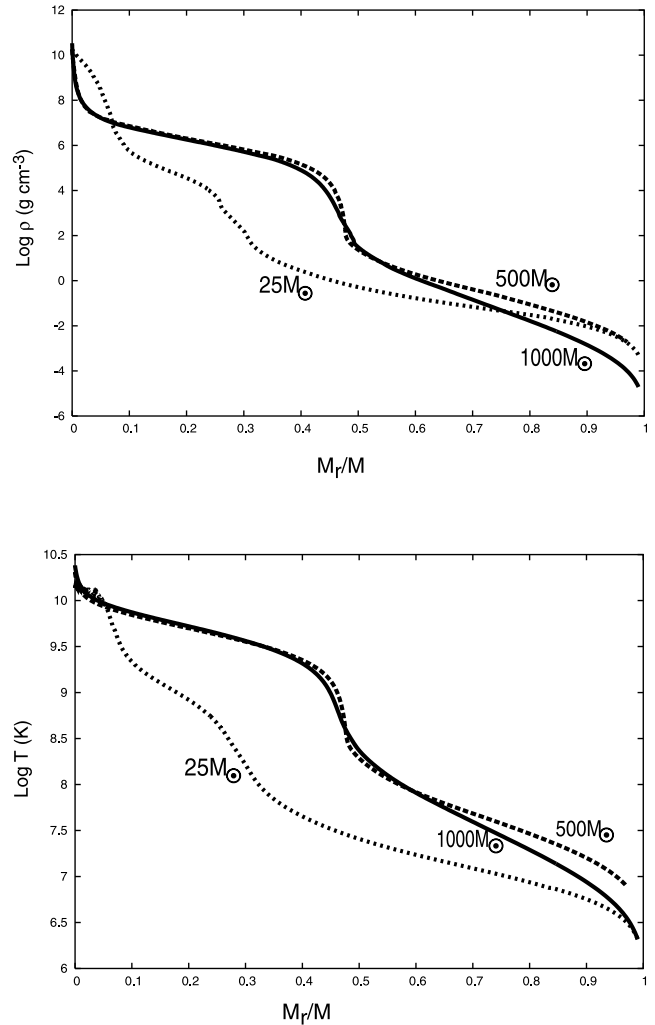


FIG. 3.—Density structure (top) and temperature structure (bottom) of 25, 500,  $1000 M_{\odot}$  models. The horizontal axis is the mass fractions  $M_r/M_{\text{tot}}$ . The vertical axis shows either the density (top) or the temperature (bottom). The data of  $25 M_{\odot}$  are from Umeda & Nomoto (2003).

ing several figures. All figures are based on the results of high-resolution models, except for Figure 4.

#### 3.2.1. Explosion Energy and Ejected Mass

In Tables 3 and 4 we summarize for each model the total explosion energy, final black hole mass, and mass of the jets. The total explosion energy is of the order of  $10^{54}$  ergs for most cases, except that in model A-4 it is of the order  $10^{53}$  ergs. Model A-4 is almost at the border between the “successful” and “failed” explosions. Actually, we also try to calculate the case that has the same parameters as model A-4 except that  $\epsilon$  and  $\mu$  are half the values of A-4 (see model F-1 in Table 5), but in this model the jet promptly falls back to the central remnant after it is injected, and hence the explosion fails. In this model the total energy is still negative, and the stellar matter moves toward the central remnant more than 200 s after the beginning of the accretion. The absolute value of gravitational binding energy over the region outside of the central  $100 M_{\odot}$  core is as high as  $10^{55}$  ergs for the  $1000 M_{\odot}$  model. In this case energy injection is too weak for the jet to proceed outward.

Table 5 summarizes the models in which the explosion ends up as a “failure.” Figure 4 shows the models in which the explosion either occurs or not, depending on the two parameters  $\theta_{\text{jet}}$

TABLE 3  
CHARACTERISTICS OF EXPLOSION MODELS IN TABLE 1

| Models<br>(1) | $E$<br>(ergs)<br>(2) | $M_{\text{BH}}$<br>( $M_{\odot}$ )<br>(3) | $M_{e0}$<br>( $M_{\odot}$ )<br>(4) | $M_{\text{jet}}$<br>( $M_{\odot}$ )<br>(5) | $M_e$<br>( $M_{\odot}$ )<br>(6) |
|---------------|----------------------|---|------------------------------------|--|---------------------------------|
| A-1 .....     | $6.7 \times 10^{54}$ | $5.0 \times 10^2$                         | $4.6 \times 10^2$                  | 44   | $5.0 \times 10^2$               |
| A-2 .....     | $2.2 \times 10^{54}$ | $4.4 \times 10^2$                         | $5.2 \times 10^2$                  | 38   | $5.6 \times 10^2$               |
| B-1 .....     | $4.9 \times 10^{54}$ | $4.6 \times 10^2$                         | $5.4 \times 10^2$                  | 1.8  | $5.4 \times 10^2$               |
| B-2 .....     | $1.6 \times 10^{54}$ | $4.8 \times 10^2$                         | $5.2 \times 10^2$                  | 0.94                                       | $5.2 \times 10^2$               |
| B-3 .....     | $2.9 \times 10^{54}$ | $2.3 \times 10^2$                         | $2.7 \times 10^2$                  | 0.90                                       | $2.7 \times 10^2$               |

NOTES.—Col. (2): Explosion energy  $E$ . Col. (3): Final black hole mass  $M_{\text{BH}}$ . Col. (4): Ejected mass excluding jet material  $M_{e0}$ . Col. (5): Mass of jet  $M_{\text{jet}}$ . Col. (6): Total ejected mass  $M_e$ .

and  $\epsilon$ . One can see that the minimum  $\epsilon$  needed for the successful explosion becomes higher if  $\theta_{\text{jet}}$  is larger, as in model A-2 and case B (most of the injected energy is given as thermal energy). Actually, explosion energies tend to be lower in such models than those in case A models with  $\theta_{\text{jet}} = 15^\circ$ . In model A-2 and case B models, the injected energy tends to diffuse into the direction apart from the polar direction, and so the jet is weak even for the polar direction.

Figure 5 shows how the jet is propagating through the star by plotting the density structures. One can see that the jet is strongly propagating in the polar direction for A-1, while for B-1 the jet is broadened toward the side directions due to the random heat motion.

The final black hole mass and ejected mass are also important. For the 500 and the 1000  $M_{\odot}$  models, these values are  $\sim 230 M_{\odot}$  and  $500 M_{\odot}$ , respectively.

### 3.2.2. Direction-dependent Features

Figure 6 shows the regions where the matter will be accreted onto the central black hole. In these panels we can see the extent of asphericity and the amount of accreting matter. These panels show the initial positions (just before the explosion) of the accreted matter. In model A-2 in which  $\theta_{\text{jet}}$  is twice ( $30^\circ$ ) the other models ( $15^\circ$ ) and case B, asphericity is weakened to some extent, and the amount of the accreting matter is less compared with the models with  $\theta_{\text{jet}} = 15^\circ$  and the same energy transformation efficiency  $\epsilon$ . For models with  $\theta_{\text{jet}} = 15^\circ$ , the stellar matter toward the direction  $\theta > \theta_{\text{jet}}$  almost accretes up to  $500 M_{\odot}$  (even a part of the helium layer) on the mass coordinate. On the other hand, in model A-2 and case B models, a large amount of matter within the  $500 M_{\odot}$  core is ejected. At the same time, if asphericity becomes weaker, the threshold efficiency for the successful explosion becomes more strict; that is, larger  $\epsilon$  is needed. This is because more energy diffuses toward the equatorial direction.

In Figure 7 we show the maximum temperatures that each mesh reaches and the densities at the maximum temperatures

for the  $z$  (polar) direction,  $\theta = 15^\circ$ ,  $\theta = 45^\circ$ . We may pay special attention to the maximum  $T_9$  for the  $\theta = 15^\circ$  and  $\theta = 45^\circ$  direction. For some models (e.g., A-1 in the left panel) with  $\theta_{\text{jet}} = 45^\circ$ , the maximum  $T_9$  does not appear within the range of these graphs, because the matter that can experience such high temperatures is in the inner region, and hence such matter all accretes in these models. However, for the other cases the inner matter is ejected and the explosive nucleosynthesis occurs even for the  $\theta = 45^\circ$  direction.

### 3.3. Explosive Nucleosynthesis

When a shock arrives the shocked region is compressed and heated, drastically raising the density and temperature, and then the explosive nucleosynthesis occurs. The products of this event are characterized by the peak temperature. We first summarize the main products at different peak temperatures and then describe the results of the calculations.

#### 3.3.1. Explosive Burning and Products

If the peak temperature  $T_{\text{peak}}$  exceeds  $5 \times 10^9$  K, NSE is realized. In such regions “complete silicon burning” occurs, and then Fe-group elements (such as Mn, Co, Fe, Ni) are produced. The main product is  $^{56}\text{Ni}$ , which eventually decays into  $^{56}\text{Fe}$ .

In the complete-silicon-burning region, at lower density for a given temperature the reaction rate decreases, and the number of free-particles may exceed the NSE value. Or, if the initial temperature is higher, free-particles become more abundant, because in NSE the number of these particles is a high-powered function of temperature. This situation is called “ $\alpha$ -rich freezeout,” and it tends to produce the Fe-group elements and nuclei to the high- $Z$  side of the peak (e.g., Thielemann et al. 1996; Arnett 1996).

If  $4 \times 10^9 \text{ K} < T_{\text{peak}} < 5 \times 10^9 \text{ K}$  *incomplete silicon burning* occurs. In such regions, Si is not all converted into the Fe-group elements but remains or is converted to the elements such as  $^{32}\text{S}$ ,  $^{36}\text{Ar}$ , and  $^{40}\text{Ca}$ .

TABLE 4  
SAME AS TABLE 3, BUT FOR THE MODELS IN TABLE 2

| Models    | $E$<br>(ergs)        | $M_{\text{BH}}$<br>( $M_{\odot}$ ) | $M_{e0}$<br>( $M_{\odot}$ ) | $M_{\text{jet}}$<br>( $M_{\odot}$ ) | $M_e$<br>( $M_{\odot}$ ) |
|-----------|----------------------|------------------------------------|-----------------------------|-------------------------------------|--------------------------|
| A-3 ..... | $4.0 \times 10^{54}$ | $5.3 \times 10^2$                  | $4.5 \times 10^2$           | 23                                  | $4.7 \times 10^2$        |
| A-4 ..... | $5.2 \times 10^{53}$ | $5.6 \times 10^2$                  | $4.3 \times 10^2$           | 9.5                                 | $4.4 \times 10^2$        |
| A-5 ..... | $3.0 \times 10^{54}$ | $5.1 \times 10^2$                  | $4.5 \times 10^2$           | 45                                  | $4.9 \times 10^2$        |
| A-6 ..... | $8.2 \times 10^{54}$ | $5.1 \times 10^2$                  | $4.6 \times 10^2$           | 34                                  | $4.9 \times 10^2$        |
| A-7 ..... | $6.1 \times 10^{54}$ | $2.4 \times 10^2$                  | $2.4 \times 10^2$           | 21                                  | $2.6 \times 10^2$        |
| B-2 ..... | $1.9 \times 10^{54}$ | $4.8 \times 10^2$                  | $5.2 \times 10^2$           | 0.95                                | $5.2 \times 10^2$        |
| B-4 ..... | $6.4 \times 10^{54}$ | $4.6 \times 10^2$                  | $5.3 \times 10^2$           | 7.4                                 | $5.4 \times 10^2$        |
| B-5 ..... | $1.8 \times 10^{54}$ | $4.7 \times 10^2$                  | $5.3 \times 10^2$           | 3.7                                 | $5.3 \times 10^2$        |

TABLE 5  
THE MODELS IN WHICH EXPLOSION DOES NOT OCCUR

| Models    | Progenitor<br>( $M_{\odot}$ ) | $M_{\text{BH0}}$<br>( $M_{\odot}$ ) | $\theta_{\text{jet}}$<br>(deg) | $\epsilon$ | $\mu$  | $F_{\text{thrm}}$ | $v_{\text{jet}}/c$ |
|-----------|-------------------------------|-------------------------------------|--------------------------------|------------|--------|-------------------|--------------------|
| F-1 ..... | 1000                          | 100                                 | 15                             | 0.001      | 0.01   | 0.01              | 0.45               |
| F-2 ..... | 1000                          | 100                                 | 30                             | 0.005      | 0.05   | 0.01              | 0.45               |
| F-3 ..... | 1000                          | 100                                 | 45                             | 0.01       | 0.1    | 0.01              | 0.45               |
| F-4 ..... | 1000                          | 100                                 | 15                             | 0.003      | 0.0015 | 0.95              | 0.45               |

If  $3 \times 10^9 \text{ K} < T_{\text{peak}} < 4 \times 10^9 \text{ K}$  explosive oxygen burning occurs, which produces  $^{28}\text{Si}$  and  $^{32}\text{S}$ , while the original  $^{16}\text{O}$  composition stays the same.

If  $2 \times 10^9 \text{ K} < T_{\text{peak}} < 3 \times 10^9 \text{ K}$  explosive carbon burning occurs, which produces  $^{20}\text{Ne}$  and  $^{24}\text{Mg}$ . The original  $^{12}\text{C}$  remains because the burning does not proceed during such a short timescale.

If  $T_{\text{peak}} < 2 \times 10^9 \text{ K}$  almost no explosive burning occurs, and so the original chemical composition realized during the hydrostatic burning phase is conserved.

### 3.3.2. Direction-dependent Features

As typical interesting cases, Figures 8–10 show the distribution of elements after the explosive nucleosynthesis for models A-1, A-2 and B-1, respectively. In each figure the top left panel shows the Fe-group elements in the polar direction. The top right panel shows the  $\alpha$ -elements in the polar direction, the bottom left panel shows the  $\alpha$ -elements at  $\theta = 15^\circ$ , and the bottom right panel shows the  $\alpha$ -elements at  $\theta = 45^\circ$ . In each model, the complete-silicon-burning region shows strong  $\alpha$ -rich freezeout. The top panel (polar direction) in each figure shows that  $^{56}\text{Ni}$  is synthesized dominantly up to  $400 M_{\odot}$  from the center. Compared with Figure 2, which shows the chemical composition just before the explosion, one can see that oxygen is consumed in the region with  $350\text{--}400 M_{\odot}$ .

For directions  $\theta = 15^\circ$  and  $\theta = 45^\circ$  the silicon and oxygen layers considerably accrete, and even a part of the helium layer accretes for  $\theta = 45^\circ$  for model A-1. On the other hand, in models A-2 and B-1 the complete-silicon-burning region still remains for  $\theta = 15^\circ$  and the oxygen layer remains for  $\theta = 45^\circ$ . This is because the shock is diffused to the equatorial directions more than model A-1.

Figure 11 shows the mass fractions of  $^{56}\text{Ni}$  and  $\alpha$ -elements for each  $\theta$  integrated over the radial direction. These figures clearly show how much matter is ejected; for example, the ejected mass of the oxygen layer can be found by seeing the mass fraction of  $^{16}\text{O}$ . For the  $\theta_{\text{jet}} = 15^\circ$  models in case A (e.g., A-1), there is no ejected matter except helium and hydrogen in the directions  $\theta > 45^\circ$  (see also Fig. 8). However, for case B and the  $\theta_{\text{jet}} = 30^\circ$  models of case A (e.g., A-2 or B-1), the  $^{56}\text{Ni}$ -synthesized and  $\alpha$ -element-rich regions are broadened to around  $\theta = 30^\circ$  and  $80^\circ$ , respectively.

### 3.3.3. Composition of Jet Material

Figure 12 shows  $[X/\text{Fe}]$  (top panel) and mass fractions (bottom panels) for the Fe-peak elements as a function of  $Y_e$ . Note that we assume the temperature of the jet material reaches higher than  $5 \times 10^9 \text{ K}$ , and therefore, it consists mostly of the Fe-group elements and  $^4\text{He}$ .

Peculiar features are seen, particularly when  $Y_e < 0.5$ . Elements Co, Cu, Ni and Zn are dramatically abundant relative to Fe (500–1000 times larger than the solar values) as shown in Figure 12. When  $Y_e < 0.5$ , the mass fraction of synthesized

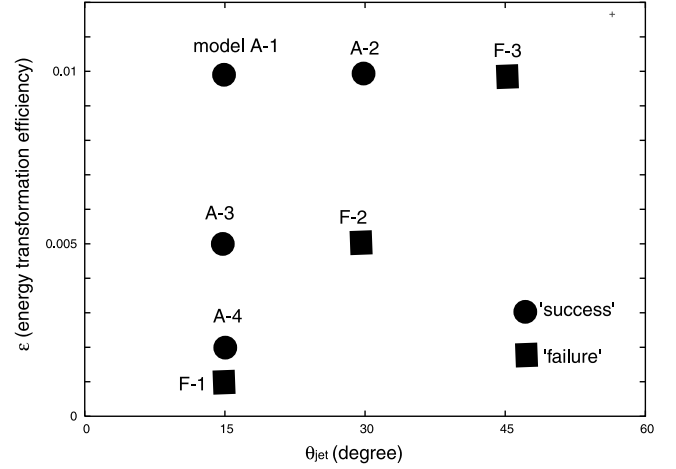


FIG. 4.—Models in which explosion occurs (circles) or does not (squares), depending on two parameters,  $\theta_{\text{jet}}$  and  $\epsilon$ , for  $1000 M_{\odot}$  models. The other parameters are set at  $\mu = 10\epsilon$ ,  $M_{\text{BH0}} = 100 M_{\odot}$ , and  $f = 0.01$  (see Tables 1, 2, and 5).

$^{56}\text{Ni}$  is very small, less than 10% for  $Y_e = 0.49$  and less than 0.1% for  $Y_e = 0.48$ . Then a large amount of neutron-rich nuclei, such as  $^{58}\text{Ni}$ ,  $^{60}\text{Ni}$ , and  $^{59}\text{Ni}$  (which decays into  $^{59}\text{Co}$ ),  $^{63}\text{Zn}$  (which decays into  $^{63}\text{Cu}$ ), and  $^{64}\text{Zn}$ , are synthesized. In these situations neutron-rich  $^{64}\text{Zn}$  is directly synthesized rather than  $^{64}\text{Ge}$ , which decays into  $^{64}\text{Zn}$ . The rise of  $[\text{Cr}/\text{Fe}]$  and  $[\text{Mn}/\text{Fe}]$  for  $Y_e < 0.5$  is mainly due to the small fraction of  $^{56}\text{Ni}$  rather than the increase of the fractions of Cr and Mn.

On the other hand, for  $Y_e > 0.5$  most of the products are  $^{56}\text{Ni}$  and  $^4\text{He}$ , similar to the case in which  $Y_e = 0.5$ . The main effect of  $Y_e > 0.5$  is the existence of free protons.

As our first step for the treatment of the jet material, Figure 13 shows the abundance pattern of jet material averaged over 15 patterns (5  $Y_e$  values times 3 entropy values).  $[\text{Zn}/\text{Fe}]$  and  $[\text{Ni}/\text{Fe}]$  are larger than the solar values due to the effects of small  $Y_e$  regions, while  $[\text{Cr}/\text{Fe}]$  and  $[\text{Mn}/\text{Fe}]$  are smaller due to the effects of large  $Y_e$  regions. The averaged mass fraction of  $^{56}\text{Ni}$  is about 40%. We multiply the mass fraction of each nucleus by the jet mass and add it to the total abundance pattern.

### 3.4. Ionization Rates, Heavy Element Yield, and Ionization Efficiency

The suggestion that VMSs are responsible for the reionization of H I and He I is not new (e.g., Gnedin & Ostriker 1997). Bromm et al. (2001) calculated the stellar atmosphere models for Pop III main-sequence CVMSs of  $300\text{--}1000 M_{\odot}$  and obtained the effective temperatures of  $\log T_{\text{eff}}(\text{K}) \sim 5.05$ , which are higher than  $\log T_{\text{eff}}(\text{K}) \sim 4.81$  of Pop I stars with the same mass and slightly higher than  $\log T_{\text{eff}}(\text{K}) = 4.85\text{--}5.0$  for Pop III  $15\text{--}90 M_{\odot}$  stars (Tumlinson & Shull 2000). Thanks to the high effective temperature, Pop III CVMSs give high production rates of ionizing radiations  $\sim 1.6 \times 10^{48} \text{ photons s}^{-1} M_{\odot}^{-1}$  for H I ionization,  $1.1 \times 10^{48} \text{ photons s}^{-1} M_{\odot}^{-1}$  for He I ionization, and  $3.8 \times 10^{47} \text{ photons s}^{-1} M_{\odot}^{-1}$  for He II ionization. These numbers correspond to  $\sim 16$ , 14 and 75 times higher, respectively, than the corresponding values with a Salpeter IMF (see Bromm et al. 2001), and therefore, they are sufficient for completely reionizing the IGM.

Daigne et al. (2004) estimate the efficiency of supplying UV photons and chemical enrichment of the IGM simultaneously. These authors suggest that the IMF that essentially forms less than  $100 M_{\odot}$  is favorable. However, this conclusion is due to the

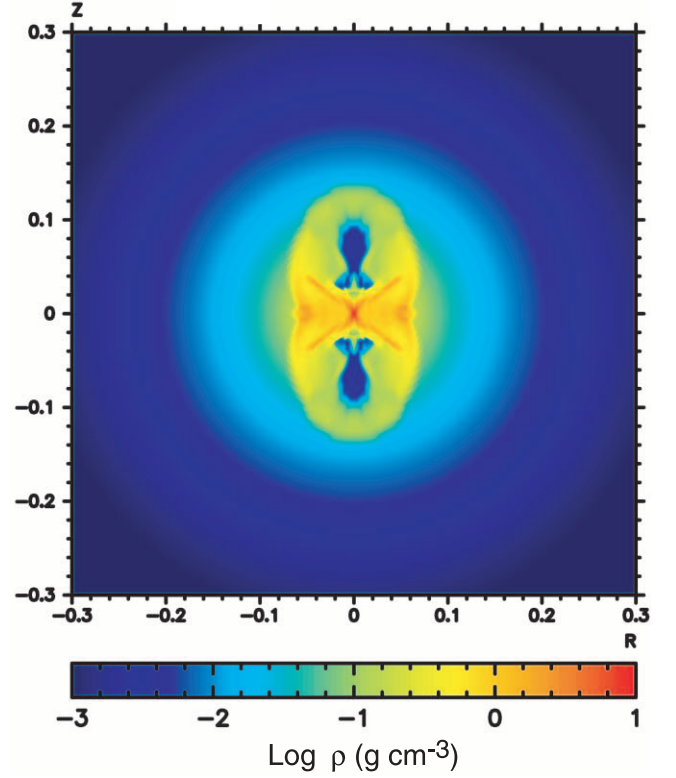
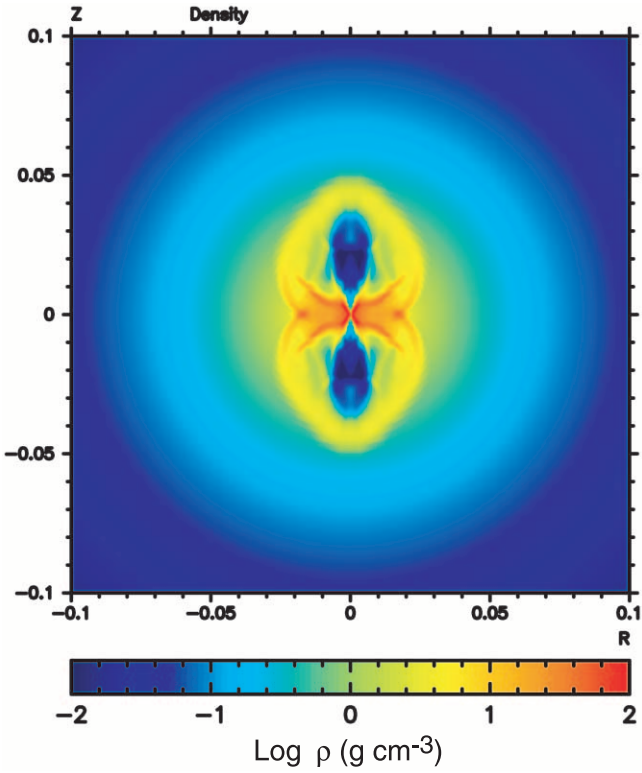
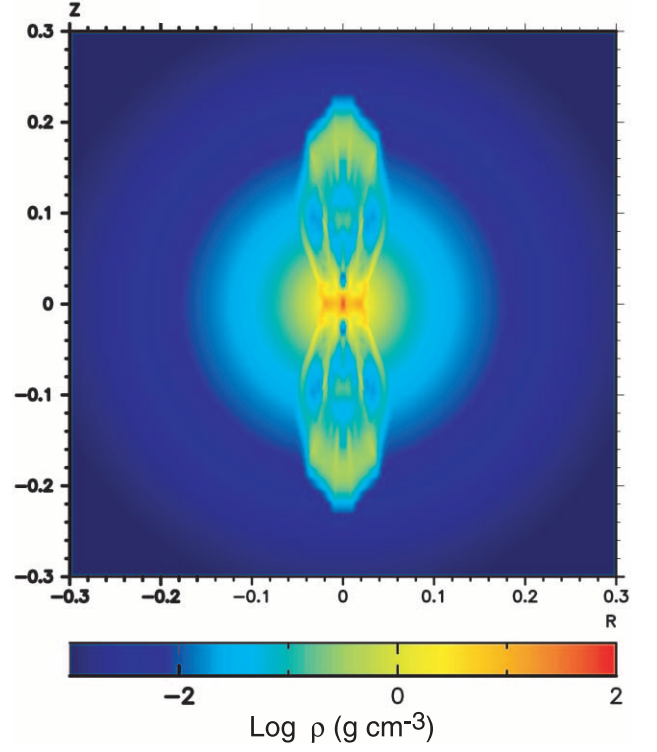
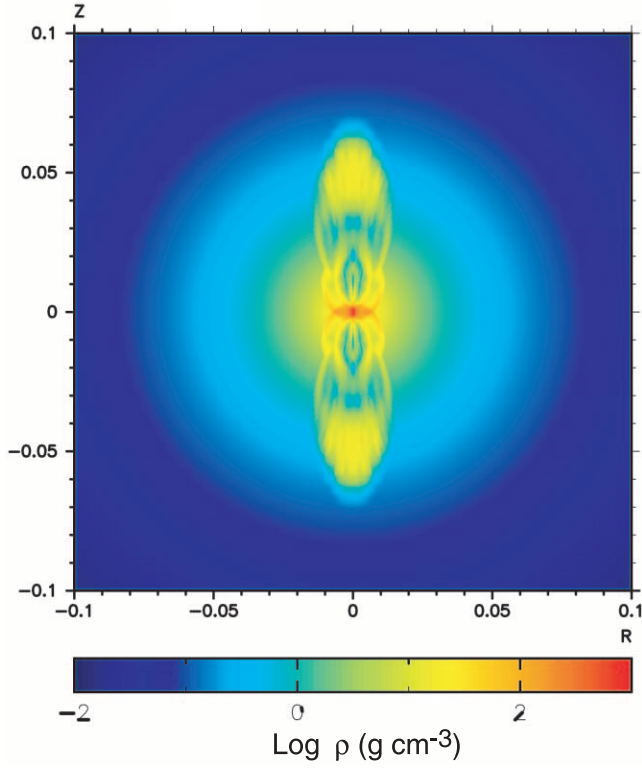


FIG. 5.—Snapshots of density structure showing how the jet is propagating at 30 s and 100 s after we started the calculation. The dial is normalized by the star's radius ( $\sim 7.7 \times 10^{12}$  cm). Note that  $\theta_{\text{jet}}$  is set at  $15^\circ$  for both models. *Top left*, 30 s (A-1); *top right*, 100 s (A-1); *bottom left*, 30 s (B-1); *bottom right*, 100 s (B-1).



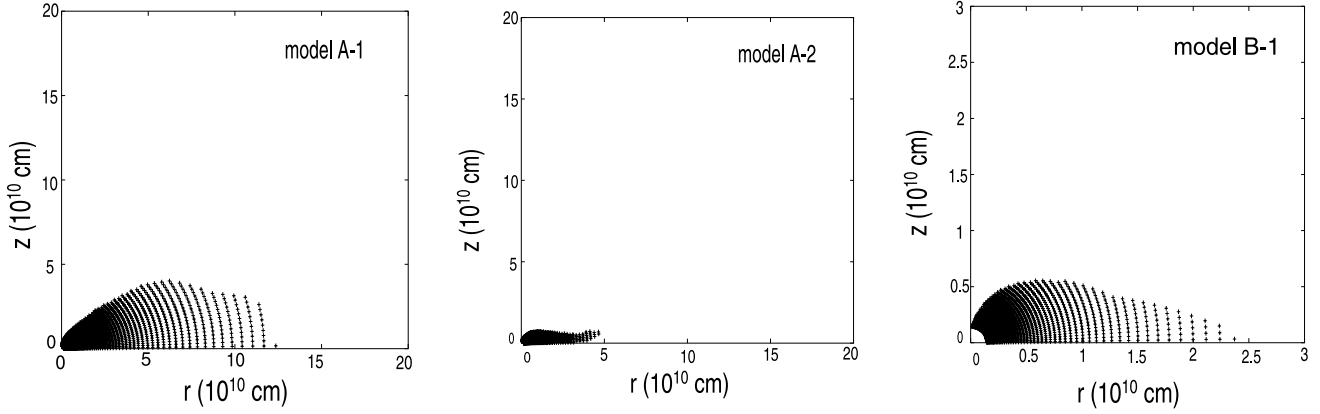


FIG. 6.—Initial radial positions of the matter that will be accreted into the central black hole for models A-1 (left), A-2 (middle), and B-1 (right). The blank region near the origin corresponds to the region of black hole initially formed.

assumption that all CVMSs collapse entirely to a black hole. Venkatesan & Truran (2003) considered the relation between the reionizing radiation and metal enrichment of the IGM, using stellar atmosphere models and model yields available at that time. For the model yields they assumed no metal ejection by stars of  $\sim 30\text{--}130 M_{\odot}$  and also  $M \gtrsim 300 M_{\odot}$ . Following their argument, here we compute the reionization efficiency for our CVMSs using model yields in the present work.

Adopting the mass of heavy elements ejected by our  $1000 M_{\odot}$  star model,  $M_Z \sim 50 M_{\odot}$ , the conversion efficiency ( $\eta_{\text{Lyc}}$ ) of energy produced in the H I ionizing radiation divided by the energy produced in the rest mass of metals ( $M_Z c^2$ ) is  $\eta_{\text{Lyc}} \sim 0.05$ . (We used eq. [1] of Venkatesan & Truran 2003.) Here we use the timescale of  $t_{\text{ms}} = 2 \times 10^6$  yr for the  $1000 M_{\odot}$  Pop III star. With these values, the number of ionizing photons per baryon in the universe generated in association with the IGM metallicity  $Z_{\text{IGM}} \sim 10^{-4}$ , obtained for our model, is  $N_{\text{Lyc}}/N_b \sim 150$ . (We used eq. [2] of Venkatesan & Truran 2003.) Note that this value well exceeds the value required for reionization of intergalactic hydrogen,  $1 < N_{\text{Lyc}}/N_b \lesssim 10$  (see Somerville et al. 2003). Therefore, contrary to the earlier results, our conclusion is that CVMSs can contribute significantly to reionization of IGM in the early epochs.

#### 4. INTEGRATED ABUNDANCE PATTERNS AND COMPARISON WITH OBSERVATIONS

The abundance pattern, the mass ratio of each element to be compared with observations, is determined by integrating the distributions over the entire ejecta regions (both radial and  $\theta$  directions). It is the mass ratio of each ejected element. Tables 6 and 7 show the ejected masses of some isotopes excluding the jet materials, and Table 8 shows the masses of all the isotopes including the jet materials.

##### 4.1. Abundance Patterns without Jet Materials

Tables 6 and 7 show the ejected mass of  $^{56}\text{Ni}$  (which decays into  $^{56}\text{Fe}$ ), excluding the jet material. Masses of  $^{16}\text{O}$  and  $^{28}\text{Si}$  are also shown as representative  $\alpha$ -elements to see the abundance and ratios of these elements. In models for case A (except model A-4), the ratios of the ejected masses of these elements to their progenitor mass are rather small, compared with those ratios in ordinary massive stars such as a  $25 M_{\odot}$  star. The typical ejected  $^{56}\text{Ni}$  mass in the  $25 M_{\odot}$  star is  $\sim 0.1 M_{\odot}$  (Maeda & Nomoto 2003). In the models with  $\theta_{\text{jet}} = 15^\circ$ , asphericity is so strong that it is only toward small  $\theta$  directions where  $^{56}\text{Ni}$  and Fe-group elements are synthesized and ejected. On the other hand, in models for case B and model A-4, these masses are much larger than the other models. The ejected  $^{56}\text{Ni}$  mass is about  $5\text{--}10 M_{\odot}$ . If this kind of supernova occurs, it is very bright in its tail, because the heating source of a supernova is  $\gamma$ -rays from radioactive decays of  $^{56}\text{Ni} \rightarrow ^{56}\text{Co} \rightarrow ^{56}\text{Fe}$ . However, it is very difficult to observe directly the explosions of first-generation stars by present observational devices, since they are very distant ( $z \gtrsim 20$ ).

##### 4.2. Total Abundance Pattern and Comparison with Observational Data

###### 4.2.1. Intracluster Matter and Hot Gas in M82

Figures 14 and 15 show the total abundance pattern for each model of higher resolution and lower resolution models, respectively, which is compared with the observational data of the ICM and M82. Note that the following discussions do not depend on the resolution. In these figures the abundance data for the ICM gas are shown with the bars (Baumgartner et al. 2005; Peterson et al. 2003), while the pentagons show the data for the gas of the central region of M82 (Ranalli et al. 2005; see also Tsuru et al. 1997). These data show that (1) the ratio  $[\text{O}/\text{Fe}]$  is smaller than

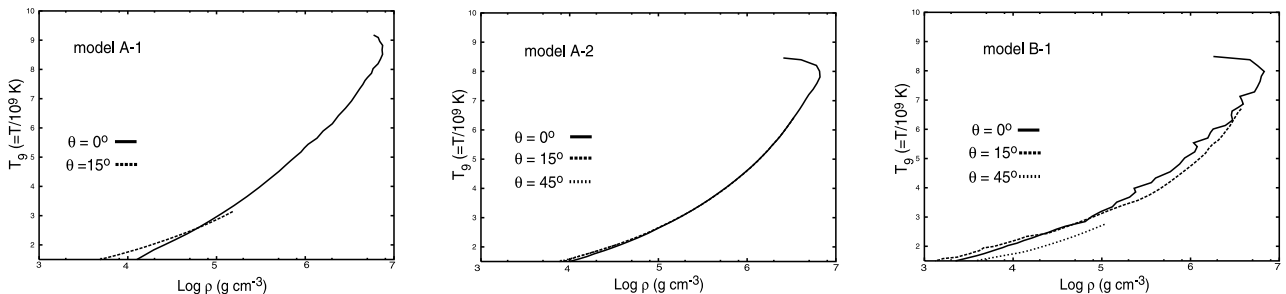


FIG. 7.—Maximum temperatures and densities of each mesh point for the directions of  $\theta = 0^\circ$ ,  $15^\circ$ , and  $45^\circ$  for models A-1 (left), A-2 (middle), and B-1 (right).

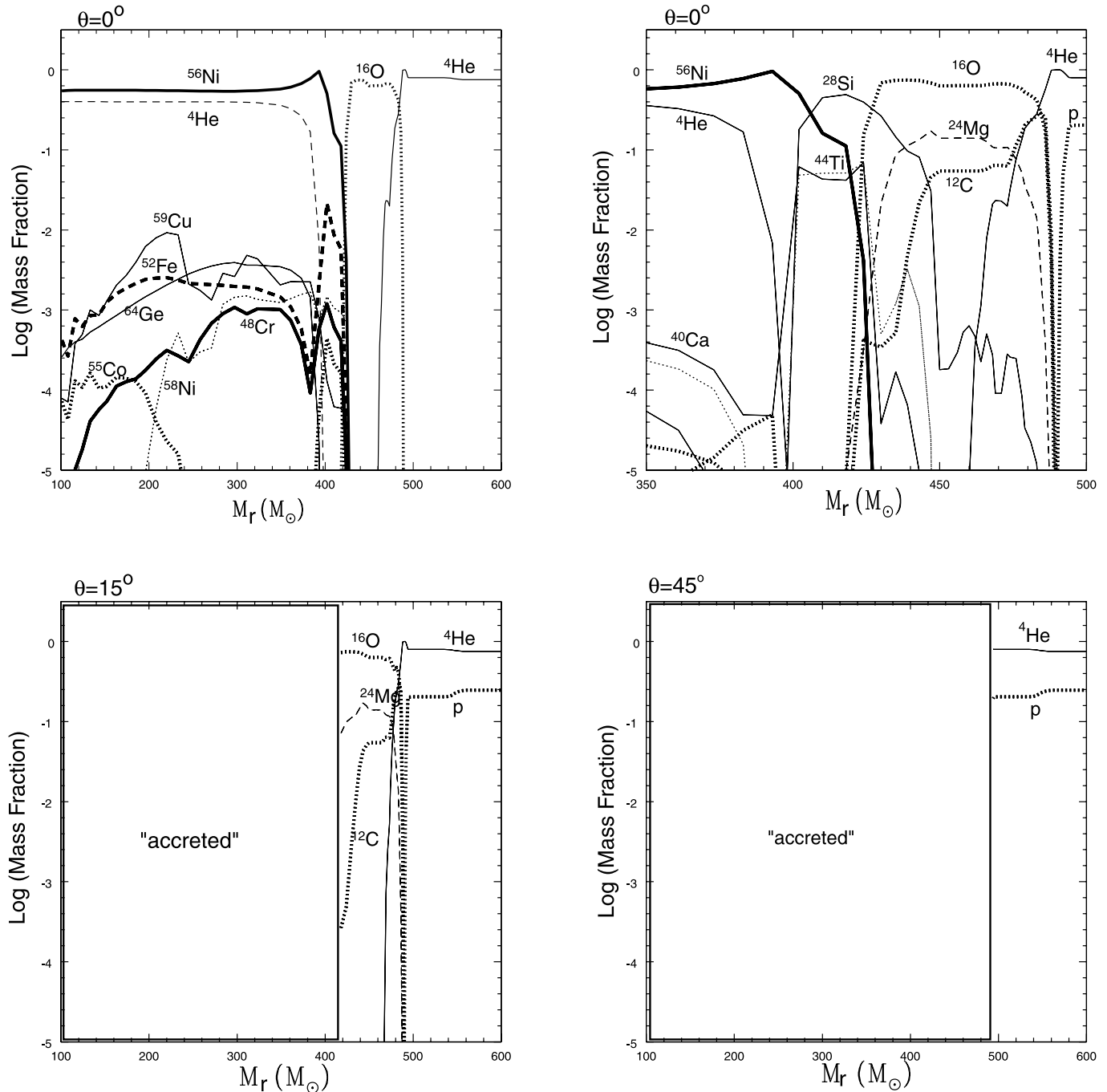


FIG. 8.—Distributions of elements: Fe-group elements for  $\theta = 0^\circ$  (top left),  $\alpha$ -elements for  $\theta = 0^\circ$  (top right),  $\alpha$ -elements for  $\theta = 15^\circ$  (bottom left), and  $\alpha$ -elements for  $\theta = 45^\circ$  (bottom right), for model A-1. Note that the mass range is set to  $350\text{--}500 M_\odot$  in the top right panel to see clearly the distributions of  $\alpha$ -elements, while in others it is set to  $100\text{--}600 M_\odot$ .

the solar value, (2)  $[\text{Ne}/\text{Fe}]$  is about the solar value, and (3) the intermediate-mass  $\alpha$ -elements such as Mg, Si, and S exhibit oversolar abundances; that is,  $[\text{Mg}/\text{Fe}]$ ,  $[\text{Si}/\text{Fe}]$ , and  $[\text{S}/\text{Fe}] \sim 0.5$  (Origlia et al. 2004; Ranalli et al. 2005).

Note that these data are not explained by standard Type II SN nucleosynthesis models. If underabundance of  $[\text{O}/\text{Fe}]$  is due to the contribution of Type Ia SNe, other  $\alpha$ -elements such as Si and S should also be underabundant. Loewenstein (2001) suggest the contribution of Pop III hypernovae (supernovae of ordinary massive stars such as  $25 M_\odot$ , with the explosion energy of at least  $\sim 10$  times larger than normal supernovae; e.g., Nomoto et al. 2003) to the enrichment of ICM, in order to explain low  $[\text{O}/\text{Fe}]$  and high  $[\text{Si}/\text{Fe}]$ , using the hypernovae mod-

els by Nakamura et al. (2001) and Heger et al. (2001). Umeda et al. (2002) also discuss this feature, but they predict smaller  $[\text{Ne}/\text{Fe}]$  and  $[\text{Mg}/\text{Fe}]$  than the data given by Ranalli et al. (2005).

Here we compare nucleosynthesis calculations of our CVMS models with these observational data. The results are summarized as follows. For our case B models we obtain the abundance pattern generally close to the observations of both ICM and M82, for example, the underabundance of  $[\text{O}/\text{Fe}]$  and  $[\text{Ne}/\text{Fe}]$  and the oversolar values of  $[\text{Mg}/\text{Fe}]$ ,  $[\text{Si}/\text{Fe}]$  and  $[\text{S}/\text{Fe}]$ . On the other hand, all case A models result in very underabundant values of  $[\alpha/\text{Fe}] \lesssim -1$ , because the mass fraction of  $^{56}\text{Ni}$  synthesized in the jet matter is much larger than that synthesized in the matter

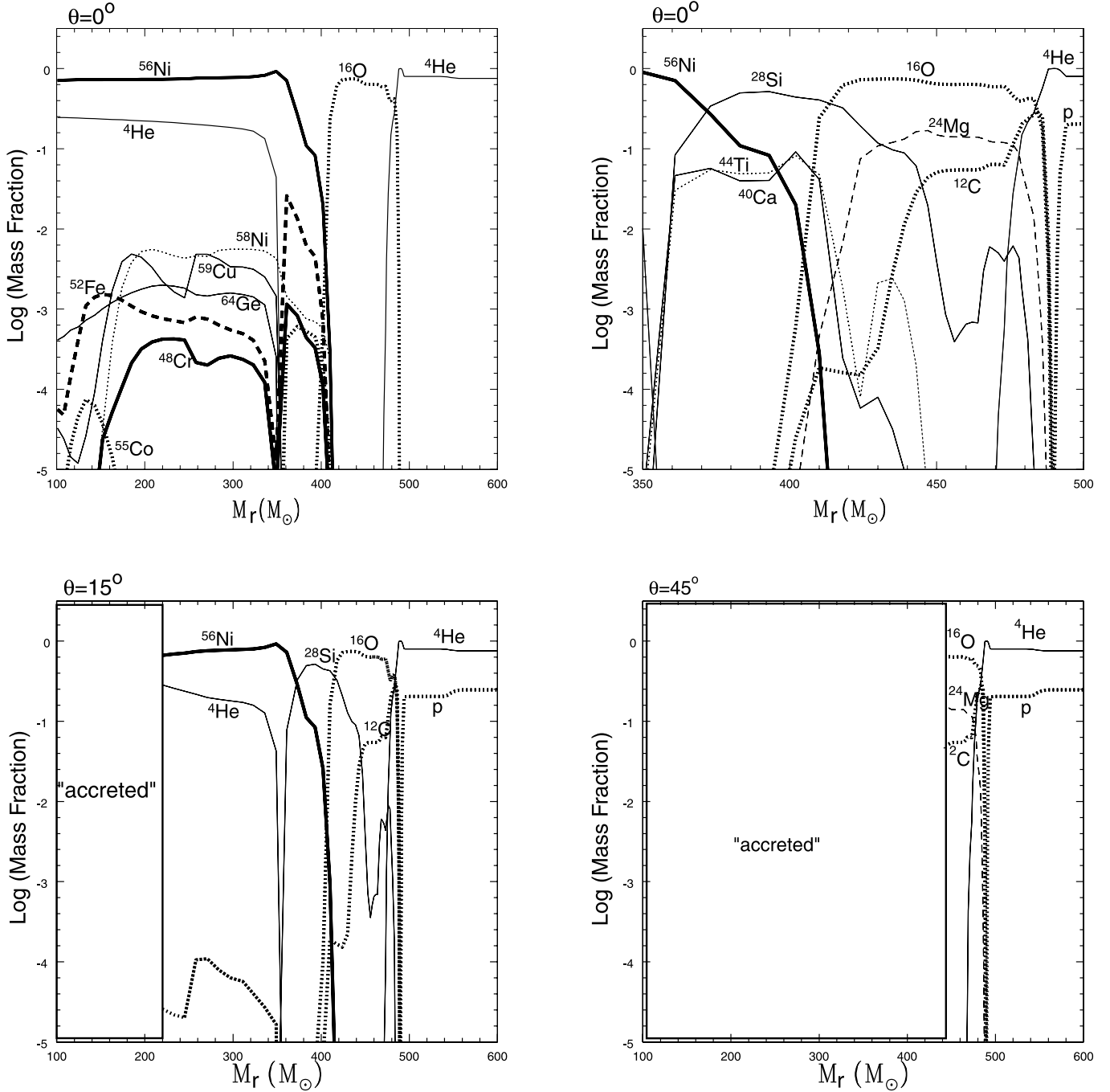


FIG. 9.—Same as Fig. 8, but for model A-2.

that does not accrete. What is more, contribution by the jet material is dominant in such models, and the uncertainty is very large. The yields of PISNe (Heger & Woosley 2002; Umeda & Nomoto 2002) are  $[O/Fe] \sim [Mg/Fe]$ ,  $[Ne/Fe] \sim 0$ , and  $[Si/Fe]$  and  $[S/Fe] \sim 1.0$ , not consistent with these data. Therefore, the yields of our case B models for CVMs can explain these abundance patterns better than those of PISNe.

#### 4.2.2. Intergalactic Medium

The abundances in the IGM at high redshift also provide important information on the early chemical evolution of the universe. Many researchers have attempted to measure the metallicity of the IGM at high redshift (Songaila & Cowie 1996; Songaila 2001; Schaye et al. 2003). Aguirre et al. (2004) ob-

serve the abundances of C and Si in the IGM at redshift  $1.5 \lesssim z \lesssim 4.5$  argue that Si and C have the same origin, and obtain  $[C/Si] \sim -0.77$ . This value is considerably lower than the yields by Population III ordinary massive stars ( $M \lesssim 40 M_\odot$ ) (see also Heger & Woosley 2002; Chieffi & Limongi 2002; Umeda & Nomoto 2002).

Matteucci & Calura (2005) discuss whether this ratio could be reproduced with their chemical evolution models and obtain  $[C/Si] = -2.0$  to  $-1.7$  by including the contribution of Pop III stars over  $100 M_\odot$ . This is too small to be compatible with the observed value. Thus, they conclude that the contribution of VMSs could not be large. However, they adopt the yields of PISNe ( $130\text{--}300 M_\odot$ ) only (Umeda & Nomoto 2002; Heger & Woosley 2002). PISNe enrich much more Si than C.

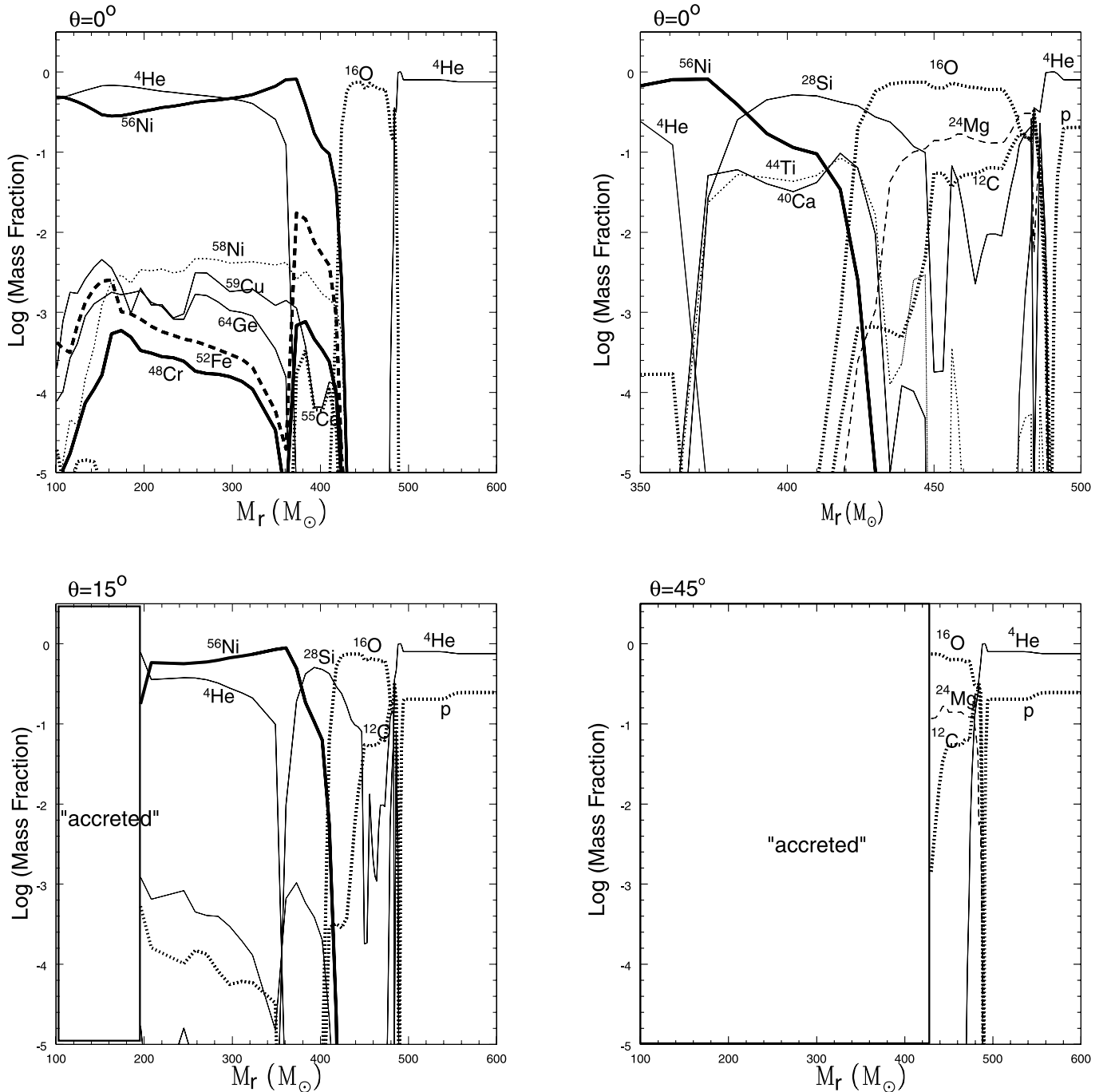


FIG. 10.—Same as Fig. 8, but for model B-1.

Although there is a similar feature between PISNe and CVMSs in that  $[C/Fe] < 0$ ,  $[Si/Fe] > 0$ , and thus  $[C/Si] < 0$ ,  $[C/Si]$  from CVMSs is not so extreme as that by PISNe. With our yields of  $1000 M_{\odot}$  CVMS,  $[C/Si] \sim -0.86$  to  $-0.68$  (including both high- and low-resolution models of  $1000 M_{\odot}$ ), which is more than 10 times larger than the results by Matteucci & Calura (2005). Our values are compatible with the observed value (Aguirre et al. 2004), and they show that the contribution of CVMS to the IGM enrichment is significant.

#### 4.2.3. Extremely Metal-poor Stars

Figure 16 compares the yields of our models with EMP stars in the Galactic halo (the data by Cayrel et al. 2004). The result is that our case B CVMS models mostly agree with these Galac-

tic halo star data for both  $\alpha$ -elements and iron-peak elements.  $[Mg/Fe]$  in the EMP stars is oversolar for a wide range of metallicity.  $[Cr/Fe]$  and  $[Mn/Fe]$  are small while  $[Co/Fe]$  and  $[Zn/Fe]$  are large. Cr (produced as  $^{48}Ti$ ) and Mn (produced as  $^{55}Co$ ) are mainly produced in the incomplete-silicon-burning region, while Co (produced as  $^{59}Cu$ ) and Zn (produced as  $^{64}Ge$ ) are mainly produced in the complete-silicon-burning region. We note that the aspherical models for ordinary massive stars with 25 and  $40 M_{\odot}$  in Maeda & Nomoto (2003) are also consistent with EMP stars' abundance patterns. Umeda & Nomoto (2003) obtain similar results with spherical models by introducing a mixing and fall-back scenario.

It has been reported that  $[O/Fe]$  is generally oversolar for EMP stars, which does not agree with our models. However, there are

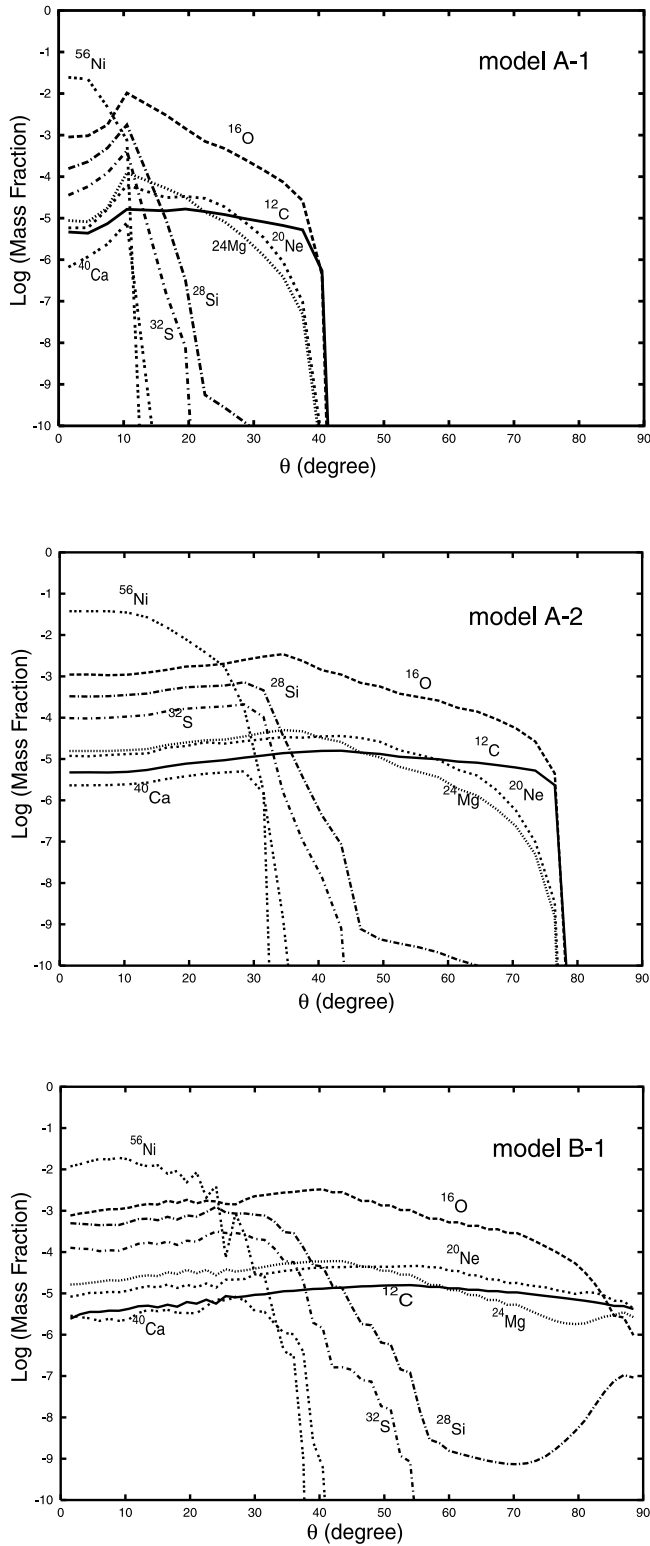


FIG. 11.—Mass fractions of ejected  $\alpha$ -elements and  $^{56}\text{Ni}$  as a function of the direction  $\theta$ . These figures are for models A-1, A-2, and B-1. These values are obtained by integrating over radial direction for each  $\theta$ .

little data for  $[\text{O}/\text{Fe}]$  at  $[\text{Fe}/\text{H}] \lesssim -3$ , and the uncertainties involved in the non-local thermal equilibrium (NLTE) effects and 3D effects may be too large to make conclusive statements. Therefore, to answer the question of whether metal-free CVMSs could contribute to the enrichment at  $[\text{Fe}/\text{H}] < -3$ , we will need more accurate observational data of  $[\text{O}/\text{Fe}]$ .

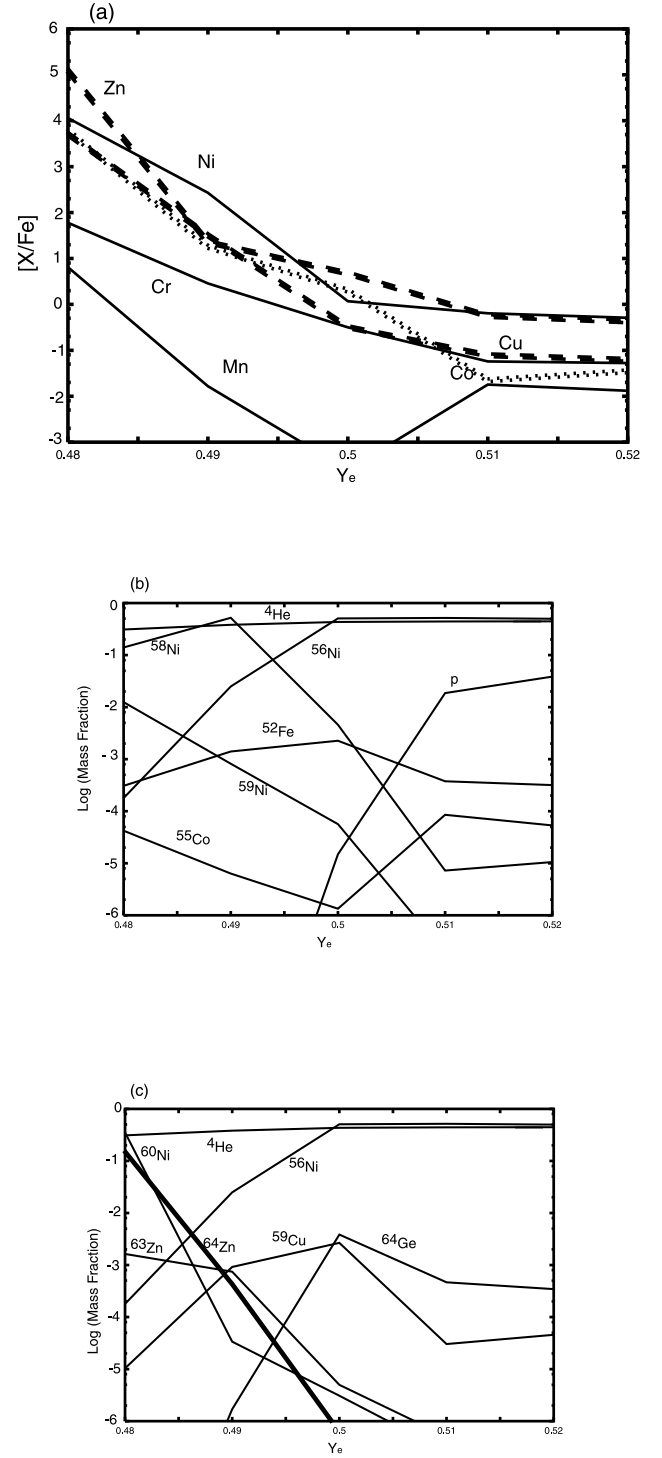
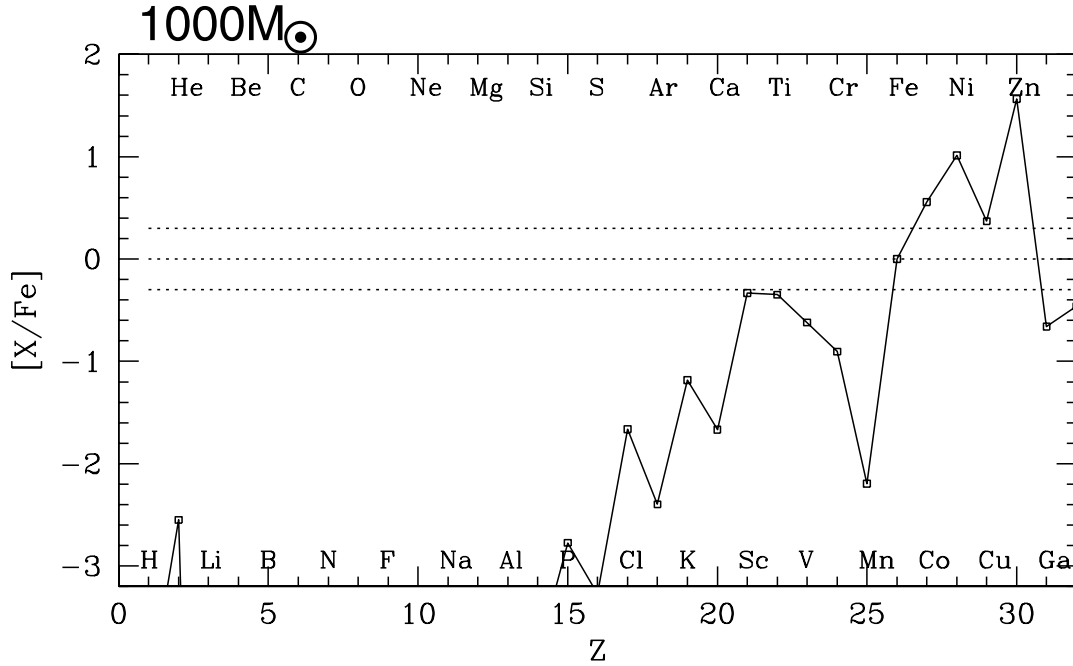


FIG. 12.—(a)  $[X/\text{Fe}]$  for Fe-group elements as a function of  $Y_e$  for history A. (b, c) Mass fractions of Fe-group elements, proton and  $^4\text{He}$  as a function of  $Y_e$  for history A. Both (b) and (c) are for history A. Some different elements are shown separately in (b) and (c) for clarity.

## 5. SUMMARY AND DISCUSSION

### 5.1. Summary

We first calculated the evolution of Pop III CVMSs with  $M = 500$  and  $1000 M_\odot$  from the pre-main sequence through the collapse with spherical symmetry. These CVMSs are thought not to explode if they undergo spherical collapse (Fryer et al. 2001). We assumed that these stars explode in a form of bipolar jets, and

FIG. 13.—Abundance pattern of jet material averaged for 15 cases ( $5 Y_e$  values times 3 density-temperature histories).

explored the required constraints. The results of our nucleosynthesis calculations were used to examine their contribution to the chemical evolution of galaxies. Our major findings are the following:

1. The region that experiences explosive silicon burning to produce iron-peak elements is more than 20% of the total mass, much larger than those of ordinary massive stars such as a  $25 M_\odot$  star. Note that for the metal-free  $25 M_\odot$  star model, this fraction is less than 10% (Umeda & Nomoto 2002). This is because for the 500 and  $1000 M_\odot$  models the density and temperature distributions are much flatter than those of  $25 M_\odot$  stars.
2. Typical explosion energy is of the order  $10^{54}$  ergs for  $1000 M_\odot$  models for the parameter ranges in this study.
3. Black hole masses are  $\sim 500 M_\odot$  for the  $1000 M_\odot$  star models. Note that such a black hole mass is very similar to those of IMBHs, e.g., a claimed  $\sim 700 M_\odot$  black hole in M82. It is quite possible that CVMSs could be the progenitors of IMBHs.
4. Nucleosynthesis yields of CVMS have similar patterns of  $[\alpha/\text{Fe}]$  to the observed abundance patterns of both ICM and gases of the central region of M82 if the contribution of the jet is small (case B). Specifically, for case B small ratios of  $[\text{O}/\text{Fe}]$  and  $[\text{Ne}/\text{Fe}]$  combined with large  $[\text{Mg}/\text{Fe}]$ ,  $[\text{Si}/\text{Fe}]$ , and  $[\text{S}/\text{Fe}]$

(i.e., large  $[(\text{Mg}, \text{Si}, \text{S})/\text{O}]$ ) are generally more consistent with these observational data than those of hypernovae and PISNe.

5. For IGM,  $[\text{C}/\text{Si}]$  of our CVMS models is compatible with that of IGM at high redshift ( $z = 5$ ), which is sufficiently higher than those of PISNe.

6. For Fe-peak elements, the main feature of the yields of our case B CVMSs is that  $[\text{Cr}/\text{Fe}]$  and  $[\text{Mn}/\text{Fe}]$  are small while  $[\text{Co}/\text{Fe}]$  and  $[\text{Zn}/\text{Fe}]$  are large. This is consistent with the observed ratios in the EMP stars. The oversolar ratios of some  $\alpha$ -elements, such as  $[\text{Mg}/\text{Fe}]$  and  $[\text{Si}/\text{Fe}]$ , are also consistent with EMP stars. Our CVMS models do not agree with the oversolar  $[\text{O}/\text{Fe}]$  of EMP stars. However, more data of  $[\text{O}/\text{Fe}]$  in EMP stars will be needed in order to see whether CVMSs can contribute to the early galactic chemical evolution. In this sense  $[\text{O}/\text{Fe}]$  would be important to discriminate between different models.

## 5.2. Discussion

### 5.2.1. Mass Accretion and Mass Loss

It was pointed out (Omukai & Palla 2003; Tan & McKee 2004) that after a protostar starts shining as a main-sequence star the accretion still continues. In our current study, as a starting

TABLE 6  
EJECTED MASS OF  $^{56}\text{Ni}$ ,  $^{16}\text{O}$ , AND  $^{28}\text{Si}$ , EXCLUDING JET MATERIAL  
FOR HIGHER RESOLUTION MODELS

| Models    | $M(^{56}\text{Ni})$<br>( $M_\odot$ ) | $M(^{16}\text{O})$<br>( $M_\odot$ ) | $M(^{28}\text{Si})$<br>( $M_\odot$ ) |
|-----------|--------------------------------------|-------------------------------------|--------------------------------------|
| A-1 ..... | 1.5                                  | 4.5                                 | 0.69                                 |
| A-2 ..... | 12                                   | 18                                  | 4.3                                  |
| B-1 ..... | 9.3                                  | 23                                  | 6.1                                  |
| B-2 ..... | 4.7                                  | 24                                  | 4.0                                  |
| B-3 ..... | 8.9                                  | 10                                  | 4.8                                  |

TABLE 7  
SAME AS TABLE 6, BUT FOR LOWER RESOLUTION MODELS

| Models    | $M(^{56}\text{Ni})$<br>( $M_\odot$ ) | $M(^{16}\text{O})$<br>( $M_\odot$ ) | $M(^{28}\text{Si})$<br>( $M_\odot$ ) |
|-----------|--------------------------------------|-------------------------------------|--------------------------------------|
| A-3 ..... | 0.4                                  | 2.1                                 | 0.24                                 |
| A-4 ..... | 0.12                                 | 1.2                                 | 0.080                                |
| A-5 ..... | 0.36                                 | 2.4                                 | 0.23                                 |
| A-6 ..... | 1.4                                  | 5.1                                 | 0.77                                 |
| A-7 ..... | 1.1                                  | 1.8                                 | 0.41                                 |
| B-2 ..... | 4.4                                  | 22                                  | 3.8                                  |
| B-4 ..... | 7.0                                  | 24                                  | 5.3                                  |
| B-5 ..... | 5.8                                  | 25                                  | 4.6                                  |

TABLE 8  
NUCLEOSYNTHESIS PRODUCTS ( $M_{\odot}$ ) OF MODELS A-1, B-1, B-2, AND B-3

| Models                 | A-1      | B-1      | B-2      | B-3      | Models                 | A-1      | B-1      | B-2      | B-3      |
|------------------------|----------|----------|----------|----------|------------------------|----------|----------|----------|----------|
| $n$ .....              | 1.68E-13 | 6.94E-12 | 5.19E-13 | 5.65E-14 | $^{50}\text{Cr}$ ..... | 1.04E-03 | 1.75E-04 | 9.71E-05 | 1.29E-04 |
| $p$ .....              | 1.90E+02 | 1.94E+02 | 1.94E+02 | 9.59E+01 | $^{51}\text{Cr}$ ..... | 1.75E-05 | 8.55E-07 | 7.88E-07 | 6.45E-07 |
| $d$ .....              | 2.78E-15 | 3.65E-15 | 2.84E-15 | 4.00E-15 | $^{52}\text{Cr}$ ..... | 3.81E-05 | 1.61E-06 | 8.16E-07 | 9.77E-07 |
| $^3\text{He}$ .....    | 2.12E-04 | 2.12E-04 | 2.12E-04 | 2.02E-05 | $^{53}\text{Cr}$ ..... | 6.53E-09 | 4.55E-10 | 2.15E-10 | 2.28E-10 |
| $^4\text{He}$ .....    | 2.72E+02 | 2.85E+02 | 2.83E+02 | 1.43E+02 | $^{54}\text{Cr}$ ..... | 4.17E-10 | 1.30E-10 | 5.06E-11 | 8.69E-11 |
| $^6\text{Li}$ .....    | 1.09E-18 | 9.64E-18 | 1.20E-17 | 6.99E-18 | $^{55}\text{Cr}$ ..... | 7.20E-12 | 1.41E-10 | 4.98E-11 | 5.59E-11 |
| $^7\text{Li}$ .....    | 2.77E-14 | 1.36E-13 | 1.52E-13 | 3.47E-14 | $^{48}\text{Mn}$ ..... | 6.84E-05 | 2.99E-06 | 1.37E-06 | 1.40E-06 |
| $^7\text{Be}$ .....    | 3.77E-09 | 3.86E-09 | 3.89E-09 | 1.86E-09 | $^{49}\text{Mn}$ ..... | 3.54E-04 | 1.12E-04 | 2.88E-05 | 6.88E-05 |
| $^9\text{Be}$ .....    | 6.40E-21 | 3.83E-19 | 3.10E-20 | 8.71E-21 | $^{50}\text{Mn}$ ..... | 2.30E-04 | 6.94E-05 | 2.08E-05 | 3.61E-05 |
| $^8\text{B}$ .....     | 2.93E-14 | 3.05E-14 | 3.05E-14 | 4.54E-13 | $^{51}\text{Mn}$ ..... | 1.16E-03 | 2.68E-04 | 9.65E-05 | 1.56E-04 |
| $^{10}\text{B}$ .....  | 7.04E-15 | 8.02E-14 | 9.11E-14 | 2.96E-14 | $^{52}\text{Mn}$ ..... | 1.09E-04 | 9.84E-06 | 7.71E-06 | 9.95E-06 |
| $^{11}\text{B}$ .....  | 1.08E-15 | 1.22E-14 | 1.20E-14 | 5.68E-15 | $^{53}\text{Mn}$ ..... | 1.66E-04 | 2.00E-05 | 1.37E-05 | 2.87E-05 |
| $^{11}\text{C}$ .....  | 1.74E-12 | 1.05E-11 | 4.28E-12 | 3.14E-12 | $^{54}\text{Mn}$ ..... | 3.20E-07 | 1.38E-08 | 6.94E-09 | 7.63E-09 |
| $^{12}\text{C}$ .....  | 8.11E-01 | 3.56E+00 | 3.68E+00 | 7.61E-01 | $^{55}\text{Mn}$ ..... | 1.73E-08 | 9.05E-10 | 4.36E-10 | 5.97E-10 |
| $^{13}\text{C}$ .....  | 6.07E-09 | 2.23E-08 | 2.30E-08 | 4.58E-08 | $^{56}\text{Mn}$ ..... | 8.12E-12 | 1.03E-10 | 4.28E-11 | 8.74E-11 |
| $^{13}\text{N}$ .....  | 1.16E-10 | 3.20E-10 | 6.14E-10 | 2.31E-08 | $^{57}\text{Mn}$ ..... | 7.48E-12 | 1.08E-10 | 4.22E-11 | 7.60E-11 |
| $^{14}\text{N}$ .....  | 1.16E-05 | 3.49E-05 | 2.77E-05 | 7.15E-06 | $^{50}\text{Fe}$ ..... | 2.01E-04 | 1.09E-05 | 3.63E-06 | 4.36E-06 |
| $^{15}\text{N}$ .....  | 3.13E-09 | 1.30E-07 | 3.93E-08 | 1.40E-07 | $^{51}\text{Fe}$ ..... | 4.36E-04 | 5.11E-05 | 9.14E-06 | 1.84E-05 |
| $^{14}\text{O}$ .....  | 2.54E-05 | 9.14E-04 | 1.86E-04 | 1.41E-04 | $^{52}\text{Fe}$ ..... | 4.31E-02 | 9.34E-02 | 5.22E-02 | 8.61E-02 |
| $^{15}\text{O}$ .....  | 2.18E-06 | 7.72E-06 | 4.25E-06 | 5.12E-06 | $^{53}\text{Fe}$ ..... | 1.36E-03 | 3.34E-03 | 2.00E-03 | 3.61E-03 |
| $^{16}\text{O}$ .....  | 4.55E+00 | 2.31E+01 | 2.37E+01 | 1.03E+01 | $^{54}\text{Fe}$ ..... | 2.26E-03 | 5.19E-03 | 4.99E-03 | 1.11E-02 |
| $^{17}\text{O}$ .....  | 1.74E-08 | 1.29E-07 | 5.67E-08 | 3.57E-08 | $^{55}\text{Fe}$ ..... | 3.96E-05 | 3.52E-06 | 2.16E-06 | 1.06E-05 |
| $^{18}\text{O}$ .....  | 2.50E-07 | 5.92E-07 | 9.19E-07 | 6.93E-11 | $^{56}\text{Fe}$ ..... | 5.40E-05 | 2.73E-06 | 1.33E-06 | 6.56E-06 |
| $^{17}\text{F}$ .....  | 1.24E-08 | 2.86E-09 | 1.58E-09 | 7.01E-10 | $^{57}\text{Fe}$ ..... | 6.49E-08 | 2.94E-09 | 1.45E-09 | 1.63E-09 |
| $^{18}\text{F}$ .....  | 8.20E-08 | 8.77E-06 | 1.25E-06 | 7.24E-07 | $^{58}\text{Fe}$ ..... | 6.00E-09 | 4.07E-10 | 1.87E-10 | 2.09E-10 |
| $^{19}\text{F}$ .....  | 6.80E-11 | 5.56E-08 | 1.37E-09 | 1.43E-08 | $^{59}\text{Fe}$ ..... | 6.49E-12 | 1.16E-10 | 5.11E-11 | 6.46E-11 |
| $^{18}\text{Ne}$ ..... | 6.92E-06 | 3.10E-07 | 1.48E-07 | 4.68E-07 | $^{60}\text{Fe}$ ..... | 7.62E-12 | 1.31E-10 | 4.37E-11 | 7.54E-11 |
| $^{19}\text{Ne}$ ..... | 2.91E-07 | 1.07E-06 | 2.77E-08 | 5.09E-07 | $^{61}\text{Fe}$ ..... | 3.56E-12 | 1.20E-10 | 2.07E-11 | 7.08E-11 |
| $^{20}\text{Ne}$ ..... | 7.83E-01 | 5.18E+00 | 4.82E+00 | 1.58E+00 | $^{51}\text{Co}$ ..... | 2.89E-10 | 1.19E-11 | 5.95E-12 | 5.71E-12 |
| $^{21}\text{Ne}$ ..... | 1.23E-05 | 2.56E-05 | 4.48E-05 | 2.35E-05 | $^{52}\text{Co}$ ..... | 1.22E-05 | 4.82E-07 | 2.27E-07 | 2.35E-07 |
| $^{22}\text{Ne}$ ..... | 1.34E-05 | 2.27E-05 | 4.64E-05 | 1.50E-06 | $^{53}\text{Co}$ ..... | 1.56E-04 | 1.39E-05 | 4.15E-06 | 6.23E-06 |
| $^{21}\text{Na}$ ..... | 4.98E-07 | 2.84E-06 | 6.22E-07 | 1.44E-06 | $^{54}\text{Co}$ ..... | 3.07E-04 | 6.25E-05 | 1.14E-05 | 3.25E-05 |
| $^{22}\text{Na}$ ..... | 1.64E-06 | 1.13E-05 | 1.53E-05 | 3.55E-05 | $^{55}\text{Co}$ ..... | 1.37E-03 | 3.30E-03 | 1.79E-03 | 4.02E-03 |
| $^{23}\text{Na}$ ..... | 4.18E-05 | 3.46E-04 | 4.14E-04 | 5.56E-04 | $^{56}\text{Co}$ ..... | 1.72E-04 | 1.89E-05 | 1.32E-05 | 1.99E-05 |
| $^{22}\text{Mg}$ ..... | 2.37E-04 | 1.58E-05 | 6.22E-06 | 1.26E-05 | $^{57}\text{Co}$ ..... | 5.33E-04 | 2.71E-05 | 1.60E-05 | 1.43E-05 |
| $^{23}\text{Mg}$ ..... | 2.14E-04 | 7.84E-04 | 9.12E-04 | 1.04E-03 | $^{58}\text{Co}$ ..... | 7.77E-06 | 3.29E-07 | 1.66E-07 | 1.60E-07 |
| $^{24}\text{Mg}$ ..... | 7.05E-01 | 4.55E+00 | 4.14E+00 | 1.43E+00 | $^{59}\text{Co}$ ..... | 3.23E-05 | 1.37E-06 | 6.89E-07 | 6.58E-07 |
| $^{25}\text{Mg}$ ..... | 1.47E-04 | 6.76E-04 | 7.04E-04 | 2.88E-04 | $^{60}\text{Co}$ ..... | 4.68E-09 | 4.20E-10 | 1.80E-10 | 2.39E-10 |
| $^{26}\text{Mg}$ ..... | 3.65E-05 | 1.70E-04 | 1.50E-04 | 4.11E-05 | $^{61}\text{Co}$ ..... | 1.82E-11 | 2.24E-10 | 8.42E-11 | 1.02E-10 |
| $^{27}\text{Mg}$ ..... | 1.54E-11 | 9.35E-10 | 1.85E-10 | 3.38E-11 | $^{62}\text{Co}$ ..... | 6.29E-12 | 1.32E-10 | 5.11E-11 | 8.78E-11 |
| $^{25}\text{Al}$ ..... | 2.97E-05 | 1.10E-04 | 1.25E-05 | 2.79E-04 | $^{54}\text{Ni}$ ..... | 5.26E-05 | 1.42E-06 | 5.54E-07 | 6.72E-07 |
| $^{26}\text{Al}$ ..... | 3.88E-06 | 1.72E-05 | 1.42E-05 | 2.54E-05 | $^{55}\text{Ni}$ ..... | 3.16E-04 | 1.57E-05 | 4.70E-06 | 5.77E-06 |
| $^{27}\text{Al}$ ..... | 5.97E-04 | 7.06E-03 | 4.95E-03 | 5.78E-03 | $^{56}\text{Ni}$ ..... | 2.04E+01 | 1.01E+01 | 5.07E+00 | 9.32E+00 |
| $^{28}\text{Al}$ ..... | 1.98E-08 | 5.58E-07 | 1.88E-07 | 9.17E-08 | $^{57}\text{Ni}$ ..... | 3.80E-01 | 1.68E-01 | 8.32E-02 | 1.30E-01 |
| $^{29}\text{Al}$ ..... | 1.42E-12 | 7.85E-11 | 1.31E-11 | 1.24E-11 | $^{58}\text{Ni}$ ..... | 7.66E+00 | 3.83E-01 | 1.93E-01 | 2.03E-01 |
| $^{26}\text{Si}$ ..... | 5.63E-04 | 7.80E-05 | 2.16E-05 | 5.95E-05 | $^{59}\text{Ni}$ ..... | 1.47E-01 | 6.79E-03 | 3.76E-03 | 3.47E-03 |
| $^{27}\text{Si}$ ..... | 2.62E-04 | 1.21E-03 | 1.06E-03 | 1.14E-03 | $^{60}\text{Ni}$ ..... | 2.31E+00 | 9.74E-02 | 5.21E-02 | 4.69E-02 |
| $^{28}\text{Si}$ ..... | 6.92E-01 | 6.19E+00 | 4.04E+00 | 4.81E+00 | $^{61}\text{Ni}$ ..... | 2.29E-03 | 9.65E-05 | 4.97E-05 | 4.65E-05 |
| $^{29}\text{Si}$ ..... | 3.07E-04 | 2.26E-03 | 1.94E-03 | 3.03E-03 | $^{62}\text{Ni}$ ..... | 2.13E-04 | 9.00E-06 | 4.64E-06 | 4.33E-06 |
| $^{30}\text{Si}$ ..... | 1.66E-05 | 2.38E-04 | 7.63E-05 | 5.81E-04 | $^{63}\text{Ni}$ ..... | 3.05E-08 | 1.40E-09 | 6.71E-10 | 6.68E-10 |
| $^{31}\text{Si}$ ..... | 4.78E-11 | 8.74E-09 | 6.55E-10 | 3.94E-09 | $^{64}\text{Ni}$ ..... | 6.81E-10 | 2.02E-10 | 9.08E-11 | 1.11E-10 |
| $^{32}\text{Si}$ ..... | 5.46E-13 | 1.14E-11 | 5.42E-12 | 3.31E-12 | $^{65}\text{Ni}$ ..... | 6.02E-12 | 1.32E-10 | 4.23E-11 | 7.07E-11 |
| $^{27}\text{P}$ .....  | 1.93E-06 | 8.17E-08 | 4.11E-08 | 3.99E-08 | $^{66}\text{Ni}$ ..... | 7.20E-12 | 2.09E-10 | 5.35E-11 | 8.03E-11 |
| $^{28}\text{P}$ .....  | 7.79E-05 | 8.57E-06 | 2.43E-06 | 3.40E-06 | $^{56}\text{Cu}$ ..... | 1.23E-09 | 5.07E-11 | 2.53E-11 | 2.45E-11 |
| $^{29}\text{P}$ .....  | 1.04E-04 | 4.08E-04 | 6.05E-05 | 1.35E-03 | $^{57}\text{Cu}$ ..... | 1.29E-03 | 5.67E-05 | 2.78E-05 | 2.87E-05 |
| $^{30}\text{P}$ .....  | 1.26E-04 | 3.25E-04 | 1.75E-04 | 2.79E-04 | $^{58}\text{Cu}$ ..... | 3.60E-02 | 4.92E-02 | 1.41E-02 | 4.46E-02 |
| $^{31}\text{P}$ .....  | 8.43E-05 | 4.22E-04 | 2.66E-04 | 7.31E-04 | $^{59}\text{Cu}$ ..... | 4.34E-02 | 3.67E-02 | 1.15E-02 | 3.46E-02 |
| $^{32}\text{P}$ .....  | 1.37E-09 | 5.33E-09 | 3.76E-09 | 1.15E-08 | $^{60}\text{Cu}$ ..... | 6.17E-03 | 3.54E-03 | 2.70E-03 | 1.71E-03 |
| $^{33}\text{P}$ .....  | 4.73E-10 | 1.16E-09 | 1.25E-09 | 4.37E-09 | $^{61}\text{Cu}$ ..... | 6.53E-02 | 2.80E-03 | 1.55E-03 | 1.35E-03 |
| $^{34}\text{P}$ .....  | 1.76E-12 | 2.02E-11 | 1.41E-11 | 2.85E-12 | $^{62}\text{Cu}$ ..... | 2.45E-03 | 1.04E-04 | 5.26E-05 | 5.00E-05 |
| $^{30}\text{S}$ .....  | 1.05E-03 | 1.58E-04 | 3.32E-05 | 7.83E-05 | $^{63}\text{Cu}$ ..... | 1.81E-03 | 7.66E-05 | 4.00E-05 | 3.69E-05 |
| $^{31}\text{S}$ .....  | 2.60E-04 | 2.94E-04 | 9.71E-05 | 1.88E-04 | $^{64}\text{Cu}$ ..... | 1.85E-06 | 7.84E-08 | 3.96E-08 | 3.78E-08 |
| $^{32}\text{S}$ .....  | 3.55E-01 | 3.17E+00 | 2.00E+00 | 2.68E+00 | $^{65}\text{Cu}$ ..... | 7.68E-07 | 3.26E-08 | 1.64E-08 | 1.57E-08 |
| $^{33}\text{S}$ .....  | 1.71E-04 | 1.11E-03 | 8.41E-04 | 1.31E-03 | $^{66}\text{Cu}$ ..... | 1.23E-10 | 1.65E-10 | 7.10E-11 | 8.85E-11 |
| $^{34}\text{S}$ .....  | 1.45E-04 | 3.39E-05 | 3.47E-05 | 3.59E-04 | $^{67}\text{Cu}$ ..... | 1.21E-11 | 2.06E-10 | 6.61E-11 | 7.34E-11 |

TABLE 8—Continued

| Models                | A-1      | B-1      | B-2      | B-3      | Models                | A-1      | B-1      | B-2      | B-3      |
|-----------------------|----------|----------|----------|----------|-----------------------|----------|----------|----------|----------|
| <i>n</i> .....        | 1.68E-13 | 6.94E-12 | 5.19E-13 | 5.65E-14 | <sup>50</sup> Cr..... | 1.04E-03 | 1.75E-04 | 9.71E-05 | 1.29E-04 |
| <sup>35</sup> S.....  | 3.83E-10 | 3.96E-10 | 4.72E-10 | 1.77E-09 | <sup>68</sup> Cu..... | 9.76E-12 | 1.65E-10 | 5.32E-11 | 6.91E-11 |
| <sup>36</sup> S.....  | 1.45E-09 | 3.52E-10 | 3.41E-10 | 2.03E-10 | <sup>59</sup> Zn..... | 1.07E-03 | 3.81E-04 | 6.15E-05 | 6.95E-04 |
| <sup>37</sup> S.....  | 1.87E-12 | 2.00E-11 | 1.48E-11 | 3.27E-12 | <sup>60</sup> Zn..... | 6.55E-01 | 3.70E-01 | 1.29E-01 | 2.08E-01 |
| <sup>32</sup> Cl..... | 4.80E-04 | 2.21E-05 | 1.02E-05 | 1.04E-05 | <sup>61</sup> Zn..... | 1.35E-02 | 2.74E-03 | 1.51E-03 | 1.78E-03 |
| <sup>33</sup> Cl..... | 9.07E-05 | 6.11E-05 | 9.32E-06 | 7.32E-05 | <sup>62</sup> Zn..... | 7.68E-01 | 3.62E-02 | 1.80E-02 | 1.93E-02 |
| <sup>34</sup> Cl..... | 2.31E-04 | 7.34E-05 | 1.68E-05 | 3.23E-05 | <sup>63</sup> Zn..... | 2.37E-02 | 1.06E-03 | 6.10E-04 | 5.23E-04 |
| <sup>35</sup> Cl..... | 3.10E-04 | 1.45E-04 | 5.12E-05 | 2.93E-04 | <sup>64</sup> Zn..... | 1.06E+00 | 4.49E-02 | 2.30E-02 | 2.16E-02 |
| <sup>36</sup> Cl..... | 2.45E-07 | 3.80E-08 | 2.64E-08 | 7.18E-08 | <sup>65</sup> Zn..... | 2.37E-03 | 1.00E-04 | 5.13E-05 | 4.82E-05 |
| <sup>37</sup> Cl..... | 1.46E-07 | 1.60E-08 | 1.35E-08 | 3.73E-08 | <sup>66</sup> Zn..... | 2.14E-03 | 9.02E-05 | 4.55E-05 | 4.34E-05 |
| <sup>38</sup> Cl..... | 3.17E-12 | 3.17E-11 | 2.95E-11 | 8.79E-12 | <sup>67</sup> Zn..... | 6.02E-07 | 2.57E-08 | 1.30E-08 | 1.24E-08 |
| <sup>34</sup> Ar..... | 1.84E-03 | 1.69E-04 | 4.99E-05 | 7.78E-05 | <sup>68</sup> Zn..... | 1.09E-08 | 6.34E-10 | 3.16E-10 | 3.11E-10 |
| <sup>35</sup> Ar..... | 8.13E-04 | 2.26E-04 | 5.11E-05 | 9.33E-05 | <sup>69</sup> Zn..... | 9.27E-12 | 2.04E-10 | 6.15E-11 | 7.40E-11 |
| <sup>36</sup> Ar..... | 6.96E-02 | 5.88E-01 | 3.65E-01 | 4.97E-01 | <sup>70</sup> Zn..... | 1.00E-11 | 2.42E-10 | 6.58E-11 | 8.77E-11 |
| <sup>37</sup> Ar..... | 5.31E-05 | 1.68E-04 | 1.16E-04 | 1.79E-04 | <sup>71</sup> Zn..... | 6.19E-12 | 1.08E-10 | 4.16E-11 | 5.50E-11 |
| <sup>38</sup> Ar..... | 3.94E-04 | 4.02E-05 | 3.34E-05 | 3.25E-04 | <sup>61</sup> Ga..... | 8.83E-05 | 3.80E-06 | 1.89E-06 | 1.84E-06 |
| <sup>39</sup> Ar..... | 7.03E-08 | 3.00E-09 | 1.53E-09 | 1.54E-09 | <sup>62</sup> Ga..... | 4.83E-05 | 5.15E-06 | 1.67E-06 | 4.16E-06 |
| <sup>40</sup> Ar..... | 8.68E-08 | 3.75E-09 | 1.89E-09 | 1.79E-09 | <sup>63</sup> Ga..... | 1.37E-03 | 1.39E-03 | 4.86E-04 | 9.56E-04 |
| <sup>41</sup> Ar..... | 2.41E-12 | 3.70E-11 | 2.57E-11 | 2.06E-11 | <sup>64</sup> Ga..... | 9.88E-04 | 4.41E-04 | 3.13E-04 | 2.06E-04 |
| <sup>42</sup> Ar..... | 2.80E-12 | 4.55E-11 | 2.62E-11 | 1.35E-11 | <sup>65</sup> Ga..... | 7.21E-04 | 3.52E-05 | 2.43E-05 | 1.63E-05 |
| <sup>43</sup> Ar..... | 4.53E-12 | 5.33E-11 | 3.00E-11 | 1.73E-11 | <sup>66</sup> Ga..... | 8.58E-05 | 3.66E-06 | 2.18E-06 | 1.77E-06 |
| <sup>36</sup> K.....  | 6.58E-04 | 3.03E-05 | 1.39E-05 | 1.39E-05 | <sup>67</sup> Ga..... | 5.36E-04 | 2.26E-05 | 1.15E-05 | 1.09E-05 |
| <sup>37</sup> K.....  | 1.11E-04 | 6.81E-05 | 1.65E-05 | 2.06E-05 | <sup>68</sup> Ga..... | 1.44E-06 | 6.12E-08 | 3.08E-08 | 2.95E-08 |
| <sup>38</sup> K.....  | 7.55E-05 | 3.07E-05 | 1.31E-05 | 9.38E-06 | <sup>69</sup> Ga..... | 1.02E-06 | 4.32E-08 | 2.18E-08 | 2.08E-08 |
| <sup>39</sup> K.....  | 6.15E-04 | 6.88E-05 | 3.66E-05 | 1.59E-04 | <sup>70</sup> Ga..... | 6.56E-10 | 2.11E-10 | 9.27E-11 | 1.24E-10 |
| <sup>40</sup> K.....  | 5.99E-07 | 2.73E-08 | 1.35E-08 | 1.65E-08 | <sup>71</sup> Ga..... | 1.99E-11 | 1.74E-10 | 7.51E-11 | 1.13E-10 |
| <sup>41</sup> K.....  | 9.58E-07 | 4.06E-08 | 2.05E-08 | 1.99E-08 | <sup>72</sup> Ga..... | 9.93E-12 | 1.38E-10 | 5.53E-11 | 7.30E-11 |
| <sup>42</sup> K.....  | 1.79E-11 | 6.95E-11 | 3.91E-11 | 3.79E-11 | <sup>73</sup> Ga..... | 1.10E-11 | 1.52E-10 | 5.98E-11 | 8.06E-11 |
| <sup>43</sup> K.....  | 7.21E-12 | 8.11E-11 | 4.19E-11 | 3.41E-11 | <sup>63</sup> Ge..... | 2.79E-05 | 1.48E-06 | 4.88E-07 | 1.60E-06 |
| <sup>44</sup> K.....  | 4.45E-12 | 7.90E-11 | 3.84E-11 | 3.77E-11 | <sup>64</sup> Ge..... | 4.06E-02 | 1.69E-02 | 7.24E-03 | 1.05E-02 |
| <sup>45</sup> K.....  | 4.16E-12 | 1.00E-10 | 3.78E-11 | 4.05E-11 | <sup>65</sup> Ge..... | 1.50E-04 | 7.10E-05 | 5.23E-05 | 4.21E-05 |
| <sup>38</sup> Ca..... | 1.42E-03 | 9.17E-05 | 3.61E-05 | 3.80E-05 | <sup>66</sup> Ge..... | 8.48E-03 | 5.55E-04 | 2.80E-04 | 3.00E-04 |
| <sup>39</sup> Ca..... | 3.00E-03 | 2.06E-04 | 7.89E-05 | 8.39E-05 | <sup>67</sup> Ge..... | 2.61E-04 | 1.18E-05 | 6.26E-06 | 5.58E-06 |
| <sup>40</sup> Ca..... | 7.03E-02 | 5.71E-01 | 3.59E-01 | 4.63E-01 | <sup>68</sup> Ge..... | 4.68E-02 | 1.98E-03 | 9.97E-04 | 9.52E-04 |
| <sup>41</sup> Ca..... | 4.81E-05 | 3.77E-05 | 2.35E-05 | 3.64E-05 | <sup>69</sup> Ge..... | 2.27E-04 | 9.59E-06 | 4.84E-06 | 4.62E-06 |
| <sup>42</sup> Ca..... | 8.38E-04 | 3.65E-05 | 1.84E-05 | 2.47E-05 | <sup>70</sup> Ge..... | 1.04E-03 | 4.38E-05 | 2.21E-05 | 2.11E-05 |
| <sup>43</sup> Ca..... | 1.55E-06 | 6.57E-08 | 3.37E-08 | 3.32E-08 | <sup>71</sup> Ge..... | 8.96E-07 | 3.81E-08 | 1.92E-08 | 1.84E-08 |
| <sup>44</sup> Ca..... | 1.14E-06 | 4.81E-08 | 2.42E-08 | 2.33E-08 | <sup>72</sup> Ge..... | 2.78E-08 | 1.41E-09 | 7.61E-10 | 6.81E-10 |
| <sup>45</sup> Ca..... | 6.55E-11 | 1.45E-10 | 5.04E-11 | 7.25E-11 | <sup>73</sup> Ge..... | 2.33E-11 | 1.63E-10 | 9.63E-11 | 8.29E-11 |
| <sup>46</sup> Ca..... | 5.62E-12 | 9.28E-11 | 5.45E-11 | 4.61E-11 | <sup>74</sup> Ge..... | 1.26E-11 | 1.53E-10 | 8.87E-11 | 8.11E-11 |
| <sup>47</sup> Ca..... | 4.46E-12 | 6.63E-11 | 3.61E-11 | 4.57E-11 | <sup>75</sup> Ge..... | 6.60E-12 | 1.63E-10 | 8.86E-11 | 5.69E-11 |
| <sup>48</sup> Ca..... | 4.01E-12 | 8.17E-11 | 4.34E-11 | 3.33E-11 | <sup>65</sup> As..... | 3.70E-09 | 1.69E-10 | 8.19E-11 | 8.45E-11 |
| <sup>40</sup> Sc..... | 8.98E-08 | 3.80E-09 | 1.91E-09 | 1.83E-09 | <sup>66</sup> As..... | 5.56E-07 | 1.83E-07 | 3.83E-08 | 5.49E-08 |
| <sup>41</sup> Sc..... | 1.51E-04 | 6.64E-06 | 3.22E-06 | 3.16E-06 | <sup>67</sup> As..... | 3.99E-05 | 1.63E-05 | 5.84E-06 | 7.92E-06 |
| <sup>42</sup> Sc..... | 2.13E-05 | 1.05E-06 | 4.67E-07 | 4.56E-07 | <sup>68</sup> As..... | 4.13E-06 | 9.82E-07 | 4.16E-07 | 4.04E-07 |
| <sup>43</sup> Sc..... | 1.43E-04 | 7.64E-06 | 3.29E-06 | 3.55E-06 | <sup>69</sup> As..... | 2.77E-06 | 1.80E-07 | 7.38E-08 | 7.03E-08 |
| <sup>44</sup> Sc..... | 1.56E-06 | 6.62E-08 | 3.34E-08 | 3.25E-08 | <sup>70</sup> As..... | 7.92E-07 | 3.38E-08 | 1.76E-08 | 1.63E-08 |
| <sup>45</sup> Sc..... | 8.43E-05 | 3.56E-06 | 1.87E-06 | 1.72E-06 | <sup>71</sup> As..... | 1.87E-05 | 7.90E-07 | 3.99E-07 | 3.80E-07 |
| <sup>46</sup> Sc..... | 3.40E-08 | 1.53E-09 | 7.62E-10 | 7.26E-10 | <sup>72</sup> As..... | 1.55E-07 | 6.74E-09 | 3.38E-09 | 3.25E-09 |
| <sup>47</sup> Sc..... | 1.45E-09 | 1.89E-10 | 7.61E-11 | 1.21E-10 | <sup>73</sup> As..... | 1.09E-07 | 4.92E-09 | 2.52E-09 | 2.37E-09 |
| <sup>48</sup> Sc..... | 5.61E-12 | 1.23E-10 | 4.45E-11 | 6.76E-11 | <sup>74</sup> As..... | 1.50E-10 | 1.38E-10 | 8.36E-11 | 9.52E-11 |
| <sup>49</sup> Sc..... | 5.77E-12 | 7.81E-11 | 5.26E-11 | 4.27E-11 | <sup>75</sup> As..... | 8.20E-11 | 2.17E-10 | 1.15E-10 | 1.39E-10 |
| <sup>42</sup> Ti..... | 5.85E-04 | 2.46E-05 | 1.22E-05 | 1.18E-05 | <sup>76</sup> As..... | 8.53E-12 | 1.35E-10 | 5.92E-11 | 6.42E-11 |
| <sup>43</sup> Ti..... | 1.23E-04 | 6.28E-06 | 2.55E-06 | 2.96E-06 | <sup>67</sup> Se..... | 2.21E-08 | 9.79E-10 | 2.79E-10 | 3.95E-10 |
| <sup>44</sup> Ti..... | 1.28E-02 | 3.30E-03 | 1.60E-03 | 2.61E-03 | <sup>68</sup> Se..... | 2.86E-04 | 4.83E-05 | 1.55E-05 | 2.52E-05 |
| <sup>45</sup> Ti..... | 7.11E-05 | 2.69E-05 | 1.52E-05 | 1.20E-05 | <sup>69</sup> Se..... | 1.26E-06 | 3.68E-07 | 1.39E-07 | 2.36E-07 |
| <sup>46</sup> Ti..... | 1.16E-03 | 6.18E-05 | 3.25E-05 | 3.07E-05 | <sup>70</sup> Se..... | 1.24E-05 | 7.52E-07 | 3.38E-07 | 4.00E-07 |
| <sup>47</sup> Ti..... | 4.09E-06 | 1.86E-07 | 5.71E-07 | 9.57E-08 | <sup>71</sup> Se..... | 1.00E-06 | 4.62E-08 | 2.26E-08 | 2.16E-08 |
| <sup>48</sup> Ti..... | 1.50E-05 | 6.32E-07 | 3.19E-07 | 3.05E-07 | <sup>72</sup> Se..... | 7.15E-04 | 3.02E-05 | 1.52E-05 | 1.46E-05 |
| <sup>49</sup> Ti..... | 1.43E-08 | 7.22E-10 | 3.61E-10 | 3.65E-10 | <sup>73</sup> Se..... | 8.71E-06 | 3.68E-07 | 1.86E-07 | 1.77E-07 |
| <sup>50</sup> Ti..... | 3.54E-11 | 1.17E-10 | 5.98E-11 | 6.37E-11 | <sup>74</sup> Se..... | 1.48E-04 | 6.27E-06 | 3.16E-06 | 3.02E-06 |
| <sup>51</sup> Ti..... | 4.88E-12 | 9.63E-11 | 3.21E-11 | 5.57E-11 | <sup>75</sup> Se..... | 9.18E-07 | 3.91E-08 | 1.98E-08 | 1.89E-08 |
| <sup>44</sup> V.....  | 3.86E-04 | 1.65E-05 | 8.17E-06 | 7.89E-06 | <sup>76</sup> Se..... | 1.77E-06 | 7.64E-08 | 3.91E-08 | 3.69E-08 |
| <sup>45</sup> V.....  | 1.57E-04 | 5.85E-05 | 1.29E-05 | 2.49E-05 | <sup>77</sup> Se..... | 2.21E-09 | 2.86E-10 | 1.28E-10 | 1.08E-10 |
| <sup>46</sup> V.....  | 7.61E-05 | 1.86E-05 | 4.71E-06 | 6.83E-06 | <sup>78</sup> Se..... | 1.88E-10 | 2.45E-10 | 1.22E-10 | 1.04E-10 |
| <sup>47</sup> V.....  | 8.10E-04 | 6.57E-05 | 2.59E-05 | 3.11E-05 | <sup>69</sup> Br..... | 4.76E-12 | 2.07E-13 | 1.03E-13 | 1.01E-13 |



TABLE 8—*Continued*

| Models                 | A-1      | B-1      | B-2      | B-3      | Models                 | A-1      | B-1      | B-2      | B-3      |
|------------------------|----------|----------|----------|----------|------------------------|----------|----------|----------|----------|
| $^{48}\text{V}$ .....  | 6.82E-05 | 2.94E-06 | 1.54E-06 | 1.47E-06 | $^{70}\text{Br}$ ..... | 1.49E-09 | 1.15E-10 | 3.49E-11 | 4.13E-11 |
| $^{49}\text{V}$ .....  | 2.86E-04 | 1.23E-05 | 7.88E-06 | 6.20E-06 | $^{71}\text{Br}$ ..... | 7.23E-07 | 4.28E-08 | 1.86E-08 | 1.93E-08 |
| $^{50}\text{V}$ .....  | 9.02E-08 | 3.98E-09 | 2.00E-09 | 1.92E-09 | $^{72}\text{Br}$ ..... | 3.45E-08 | 3.46E-09 | 1.46E-09 | 1.89E-09 |
| $^{51}\text{V}$ .....  | 2.34E-07 | 1.00E-08 | 5.03E-09 | 4.87E-09 | $^{73}\text{Br}$ ..... | 5.42E-08 | 1.07E-08 | 3.20E-09 | 5.88E-09 |
| $^{52}\text{V}$ .....  | 2.79E-11 | 8.86E-11 | 5.14E-11 | 6.41E-11 | $^{74}\text{Br}$ ..... | 9.04E-09 | 1.78E-09 | 8.19E-10 | 8.46E-10 |
| $^{53}\text{V}$ .....  | 7.36E-12 | 1.15E-10 | 5.36E-11 | 5.58E-11 | $^{75}\text{Br}$ ..... | 2.73E-07 | 1.54E-08 | 7.13E-09 | 7.77E-09 |
| $^{46}\text{Cr}$ ..... | 7.13E-04 | 3.69E-05 | 1.53E-05 | 1.68E-05 | $^{76}\text{Br}$ ..... | 1.03E-07 | 5.96E-09 | 2.71E-09 | 2.93E-09 |
| $^{47}\text{Cr}$ ..... | 3.21E-04 | 4.92E-05 | 9.88E-06 | 2.15E-05 | $^{77}\text{Br}$ ..... | 1.14E-06 | 4.94E-08 | 2.50E-08 | 2.38E-08 |
| $^{48}\text{Cr}$ ..... | 1.70E-02 | 8.42E-03 | 4.31E-03 | 7.13E-03 | $^{78}\text{Br}$ ..... | 7.85E-09 | 1.31E-09 | 4.93E-10 | 7.45E-10 |
| $^{49}\text{Cr}$ ..... | 7.06E-04 | 3.71E-04 | 1.86E-04 | 2.60E-04 | $^{79}\text{Br}$ ..... | 6.43E-09 | 1.66E-09 | 1.12E-09 | 7.53E-10 |

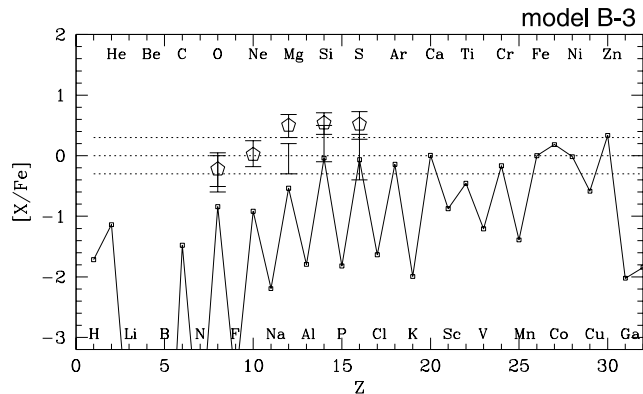
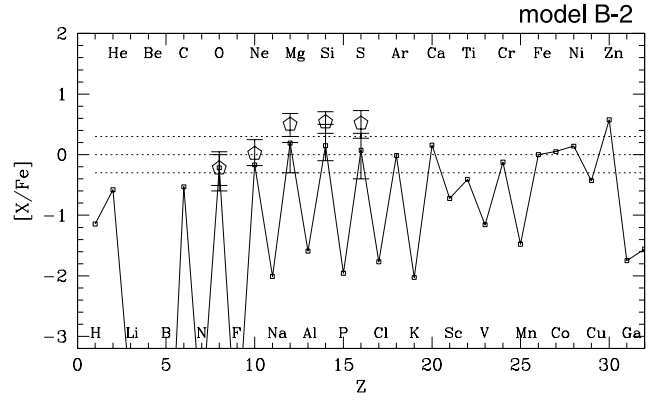
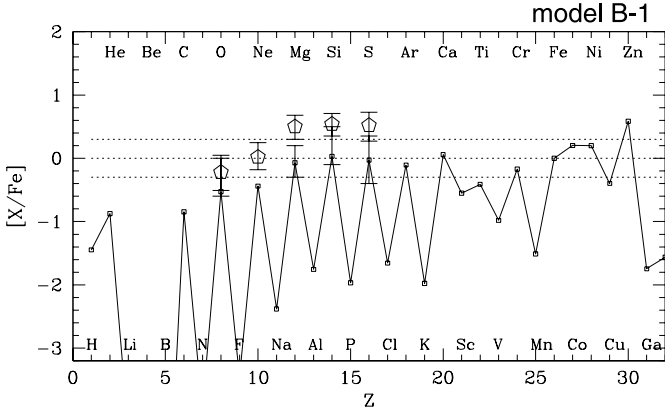
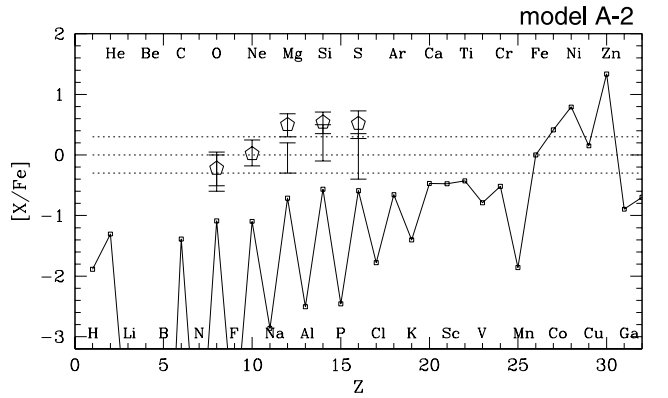
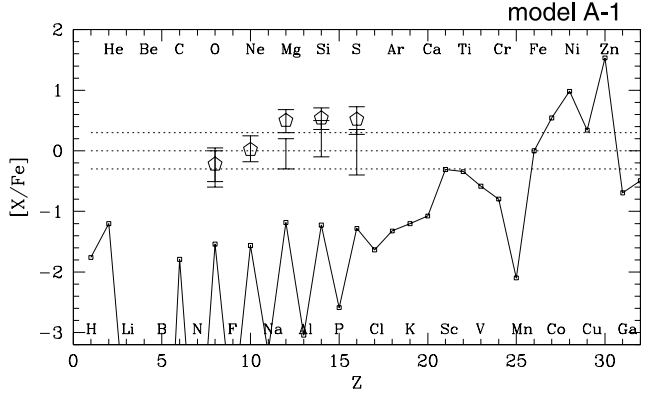


FIG. 14.—Total abundance patterns including jet contribution for higher resolution models. The open pentagons show the abundance ratios of gas of the central region in M82 (Ranalli et al. 2005). The bars show the range of abundance ratios observed in ICM (Baumgartner et al. 2005; Peterson et al. 2003).

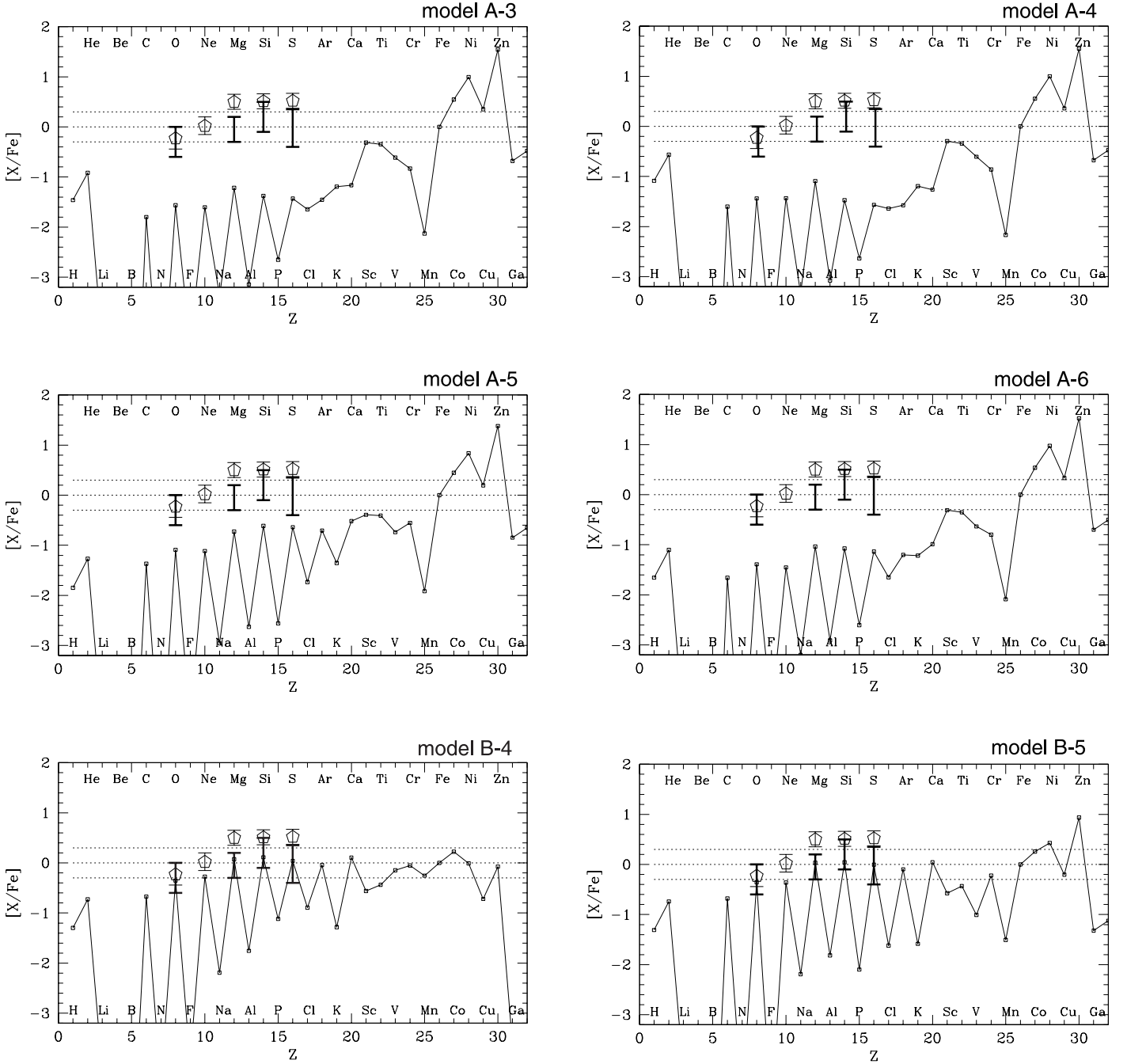


FIG. 15.—Same as Fig. 14, but for lower resolution models.

point the effect of accretion on mass growth during the pre-supernova evolution is not included. In our next, more realistic models such accretion will also be included in the evolutionary calculations. However, Omukai & Palla (2003) find that when the protostar simulation of very massive stars is carried out properly with time-dependent accretion rates, the rates generally decrease toward the end of the protostar era and after the onset of the main-sequence stellar phase.

It was also pointed out (Maeder & Meynet 2004) that mass loss will not be negligible even for zero-metallicity stars when they are rotating, and hence mass loss will also be included in the next step of our models. However, we expect that our major conclusions as summarized above are still valid, at least qualitatively. Somewhat more massive CVMSs, however, may

be needed to obtain the same mass black holes if mass loss is significant.

### 5.2.2. Reionization and Chemical Enrichment

For our CVMSs, the timescale of evolution from the zero-age main sequence to core-collapse is  $\sim 2 \times 10^6$  yr, only 1/3–1/10 as long as for ordinary massive stars ( $13\text{--}25 M_{\odot}$ ). So if these CVMSs were formed as the first-generation stars, they would be the first contributor to reionize and enrich the universe (Omukai & Palla 2003; Tumlinson & Shull 2000; Bromm et al. 2001; Schaerer 2002).

Concerning the existence of VMSs, it was proposed (e.g., see Wasserburg, & Qian 2000; Qian et al. 2002; Qian & Wasserburg 2002) that the prompt inventory involving VMSs produced the

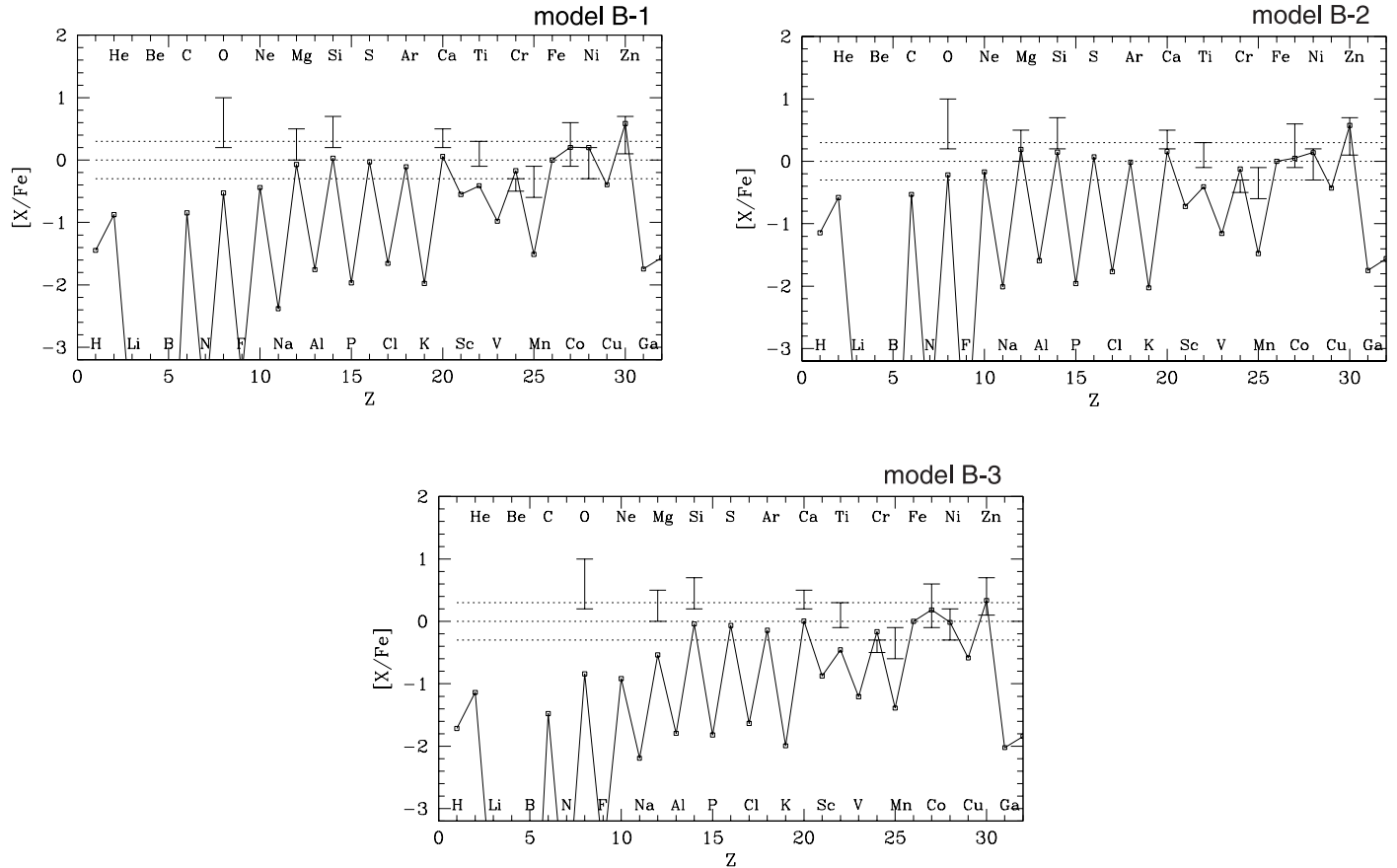


FIG. 16.—Total abundance patterns including jet contribution for case B. The bars show the observational ranges of EMP stars' abundances in Galactic halo (Cayrel et al. 2004).

elements from C to the Fe group, in order to explain the observed jump in the abundances of heavy  $r$ -process elements at  $[\text{Fe}/\text{H}] \sim -3$ , and also that while VMSs themselves produced no heavy  $r$ -elements, these stars dominated chemical evolution earlier at  $[\text{Fe}/\text{H}] < -3$ . Some others (e.g., Venkatesan & Truran 2003; Tumlinson et al. 2004) argue that various observational data on reionization, the microwave background, the metal enrichment of the high-redshift IGM, etc., indicate that the IMF of the first stars need not necessarily have been biased toward high masses. In what follows, we revisit this issue on the basis of our present models.

In § 3.4 we estimated the ionization efficiency of our CVMSs. It was found that the number of ionizing photons per baryon in the universe, generated in association with the IGM metallicity  $Z_{\text{IGM}} \sim 10^{-4}$ , is  $N_{\text{Ly}\alpha}/N_b \sim 150$ , and so CVMSs can contribute significantly to reionization of IGM in the early epoch. Here we emphasize that our current result for CVMS is contributed from the mass range with  $\sim 300\text{--}1000 M_{\odot}$ , and hence the PISN range is not included. On the other hand, Venkatesan & Truran (2003) give  $N_{\text{Ly}\alpha}/N_b \sim 10$  for  $Z_{\text{IGM}} \sim 10^{-4}$  for the mass range  $\sim 100\text{--}1000 M_{\odot}$ , which reflects the large contribution of PISNe to metal enrichment. Daigne et al. (2004) also considered reionization and chemical enrichment of IGM simultaneously and reached a similar conclusion that VMSs are not necessary. However, in their models CVMSs do not explode. Here we may note that less massive Pop III stars ( $\lesssim 100 M_{\odot}$ ) can also produce the amount of ionizing photons per metal similar to CVMSs (Venkatesan & Truran 2003; Tumlinson et al. 2004).

The relation between reionization and metal enrichment of the IGM becomes clearer if we solve the equation for  $N_{\text{Ly}\alpha}/N_b$

(eq. [2] of Venkatesan & Truran 2003) for a given value of  $Z_{\text{IGM}}$ . For a  $1000 M_{\odot}$  star,  $Z/Z_{\odot} \sim 10^{-3.4}$  and  $10^{-4.4}$  for the required number of ionizing photons per baryon 10 and 1, respectively. This is about 1 order of magnitude smaller than the case for the mass range  $100\text{--}1000 M_{\odot}$  (mainly contributed by PISNe). The difference between CVMSs and PISNe is larger if we consider the enrichment of iron. The  $260 M_{\odot}$  PISN of Heger & Woosley (2002) gives  $Z_{\text{Fe}}/Z_{\text{Fe},\odot} \sim 10^{-2}$  to  $10^{-3}$ , while our  $500$  and  $1000 M_{\odot}$  star gives  $\sim 10^{-3.2}$  to  $10^{-4.2}$ .

A main critique against the existence of PISNe comes from the fact that we do not see the abundance patterns of PISNe in EMP stars (Umeda & Nomoto 2002; Tumlinson et al. 2004). The EMP abundances are indeed suggested to be accounted for by hypernovae or faint supernovae of less massive stars of  $\lesssim 100 M_{\odot}$  (Umeda & Nomoto 2003). However, the apparent lack of evidence of VMSs by no means contradicts the existence of CVMSs at earlier epochs, if the majority of first stars in the earlier epoch has masses  $\gtrsim 300 M_{\odot}$ . First, PISNe from stars of  $\lesssim 300 M_{\odot}$  will be just a minor fraction in such a case, explaining the lack of the signature of PISNe. Second,  $Z/Z_{\odot}$  expected from our CVMSs is smaller than PISNe. Namely, the metal enrichment by CVMSs might be finished before ordinary core-collapse SNe become dominant. Note that the abundance, especially of oxygen, in EMP stars and IGM is different. Here we have shown that the yields of our CVMSs can reproduce the abundance of IGM (§ 4). Therefore, it would be worthwhile to study a scenario in which CVMSs are first formed in pregalactic mini halos, and then subsequently ordinary core-collapse SNe took place in the Galactic halo.

We mentioned that the early universe would have been too contaminated if there were many PISNe. This conclusion is not

affected when the calculation of PISNe considers the effect of rotation and asymmetric explosion (see Stringfellow & Woosley 1988). In PISNe with rotation, all matter is ejected with nothing left as in nonrotating models, and the total amount of matter ejected is almost independent of the geometry of the explosion, whether spherical or not. The explosive nucleosynthesis itself and hence the resulting exact composition of the ejected matter change with rotation and under the consequent asymmetric environment, but that does not change our conclusion that too many of PISNe result in the overabundance of heavy elements in the early universe, which contradicts the observation.

### 5.2.3. Initial Mass Function

Tumlinson et al. (2004) raised two problems associated with top heavy IMF of the first stars. (1) If stars are all  $M \gtrsim 300 M_{\odot}$ , no metals are released from Pop III stars to trigger the transition from the first stars to present IMF star formation, and (2) no mechanism has been proposed for forming stars more massive than  $\sim 300 M_{\odot}$  without forming PISNe.

Here we discuss how our CVMS models could resolve these apparent problems. Concerning problem (1), our present CVMS models do eject metals (although less than PISNe), leading to metal enrichment of IGM. In this connection, note that the existing literature concerning the effects of VMSs (in Pop III IMF) on reionization, etc., includes only contribution by PISNe but not those heavier, because Tumlinson et al. (2004) assumed that heavier stars do not explode, and hence make no contribution. However, we emphasize the importance of the explosion of these heavier stars ( $\gtrsim 500 M_{\odot}$ ).

Concerning problem (2), collisions and merging of ordinary massive stars in very dense clusters are expected to lead to the formation of more massive stars (Ebisuzaki et al. 2001; Portegies Zwart et al. 1999, 2004, Portegies Zwart 2006), which can easily lead to CVMSs ( $\gtrsim 300 M_{\odot}$ ) with or without only minor fraction of stars responsible for PISNe ( $\lesssim 300 M_{\odot}$ ), and hence the problem in question can disappear. Specifically, in this scenario PISN stars will have no time to explode before merging into heavier stars when the timescale of the PISN star evolution is longer than merging timescale. In addition, even in the case of single star formation (no merging) there is yet no reason to exclude a possibility of the first star IMF with the minimum mass of  $\sim 300 M_{\odot}$ .

As to the question of how CVMSs are formed, the first-generation stars are generally thought to have formed in low-mass halos with the virial temperature  $T_{\text{vir}} < 10^4$  K. Then the upper limit to the mass of the first stars may be  $\sim 300 M_{\odot}$  (e.g., Bromm & Loeb 2004). However, Oh & Haiman (2002) investigated halos with higher mass, with  $T_{\text{vir}} > 10^4$  K. The evolu-

tion of these high-mass halos, e.g., of  $\sim 10^9 M_{\odot}$ , is found to be quite different from the low-mass case, and the degree of fragmentation of the gas is still highly uncertain. Therefore, it appears that whether more massive stars can be directly formed is still an open question. However, regardless of the feasibility of direct formation, it has been emphasized by, e.g., Ebisuzaki et al. (2001), Portegies Zwart et al. (1999, 2004), and Portegies Zwart (2006), that CVMSs will be formed easily by merging of less massive stars in very dense star clusters, and hence there appears to be essentially no problem for CVMS formation.

### 5.2.4. Black Hole Mass

As to the existence of IMBHs, currently extensive effort is under way to try to detect them in nearby galaxies (see, e.g., Barth et al. 2005 for recent review). Already, several of these objects have been identified, mostly in dwarf elliptical galaxies but some in spiral galaxies, e.g., M33, IC 342, Pox 52, NGC 4395, and several galaxies in the Sloan Digital Sky Survey (SDSS) sample. For example, the black hole mass obtained for M33 is less than  $\sim 3000 M_{\odot}$  but larger than the mass of a stellar-mass black hole. The black hole mass obtained for NGC 4395 is  $\sim 10^4$ – $10^5 M_{\odot}$ , but its spectra are unlike NLSI (narrow-line Seyfert I), a class of AGN that tends to have a small mass. We expect more of these IMBH candidates, with better mass measurement, to be identified in the very near future.

As an example of possibly more recently formed IMBHs, Matsumoto et al. (2001) report the possible discovery of a  $\gtrsim 700 M_{\odot}$  black hole in M82 as an ULX (ultraluminous X-ray source). Since a ULX was first detected in 1989 by the *Einstein Observatory* (Fabbiano 1989), many of these objects have been discovered. Possible scenarios for formation of IMBHs associated with ULXs are speculated in a recent article by Krolik (2004). Colbert & Mushotzky (1999) first suggested that these luminous objects are indeed IMBHs, because their luminosity is super-Eddington for stellar-mass black holes if spherical accretion is adopted. That may not be necessary if beaming, etc., is assumed. However, ULXs may be heterogeneous, and at least some of these objects may well prove to be IMBHs. The prospect is bright because various observations in multifrequency bands can distinguish between different interpretations.

This work has been supported in part by the Grant-in-Aid for Scientific Research (15204010, 16540229, 17030005, 17033002) and the 21st Century COE Program (QUEST) from the JSPS and MEXT of Japan. We thank the referee for useful comments.

## REFERENCES

- Abel, T., Bryan, G. L., & Norman, M. L. 2000, *ApJ*, 540, 39  
Aguirre, A., Schaye, J., Kim, T.-S., Theuns, T., Rauch, M., & Sargent, W. L. W. 2004, *ApJ*, 602, 38  
Arnett, W. D. 1996, *Supernovae and Nucleosynthesis* (Princeton: Princeton Univ. Press)  
Baraffe, I., Heger, A., & Woosley, S. E. 2001, *ApJ*, 550, 890  
Barth, A. J., Green, J. E., & Ho, L. C. 2005, in *Growing Black Holes*, ed. A. Merloni, S. Nayakshin, & R. A. Sunyaev (Berlin: Springer), 154  
Baumgartner, W. H., Loewenstein, M., Horner, D. J., & Mushotzky, R. F. 2005, *ApJ*, 620, 680  
Bender, R. 2005, in *Growing Black Holes*, ed. A. Merloni, S. Nayakshin, & R. A. Sunyaev (Berlin: Springer), 147  
Bond, J. R., Arnett, W. D., & Carr, B. J. 1984, *ApJ*, 280, 825  
Bromm, V., Coppi, P. S., & Larson, R. B. 2002, *ApJ*, 564, 23  
Bromm, V., Kudritzki, R. P., & Loeb, A. 2001, *ApJ*, 552, 464  
Bromm, V., & Loeb, A. 2003, *ApJ*, 596, 34  
———. 2004, *NewA*, 9, 353  
Cayrel, R., et al. 2004, *A&A*, 416, 1117  
Chieffi, A., & Limongi, M. 2002, *ApJ*, 577, 281  
Colbert, E. J., & Mushotzky, R. 1999, *ApJ*, 519, 89  
Daigne, F., Olive, K. A., Vangioni-Flam, E., Silk, J., & Audouze, J. 2004, *ApJ*, 617, 693  
Ebisuzaki, T., et al. 2001, *ApJ*, 562, L19  
Fabbiano, G. 1989, *ARA&A*, 27, 87  
Fryer, C. L., Woosley, S. E., & Heger, A. 2001, *ApJ*, 550, 372  
Glatzel, W., Fricke, K. J., & El Eid, M. F. 1985, *A&A*, 149, 413  
Gnedin, N. Y., & Ostriker, J. P. 1997, *ApJ*, 486, 581  
Hachisu, I., Matsuda, T., Nomoto, K., & Shigeyama, T. 1992, *ApJ*, 390, 230  
———. 1994, *A&AS*, 104, 341  
Heger, A., Baraffe, I., Fryer, C. L., & Woosley, S. E. 2001, *Nucl. Phys. A*, 688, 197  
Heger, A., & Woosley, S. E. 2002, *ApJ*, 567, 532  
Hix, W. R., & Thielemann, F.-K. 1996, *ApJ*, 460, 869

- Ibrahim, A., Boury, A., & Noels, A. 1981, *A&A*, 103, 390
- Khokhlov, A. M., Höflich, P. A., Oran, E. S., Wheeler, J. C., Wang, L., & Chtchelkanova, A. Y. 1999, *ApJ*, 524, L107
- Kogut, A., et al. 2003, *ApJS*, 148, 161
- Kormendy, J., & Richstone, D. 1995, *ARA&A*, 33, 581
- Krolik, J. H. 2004, *ApJ*, 615, 383
- Kudritzki, R.-P. 2000, in *The First Stars*, ed. A. Weiss, T. G. Abel, & V. Hill (Berlin: Springer), 127
- Loewenstein, M. 2001, *ApJ*, 557, 573
- MacFadyen, A. I. 2003, in *From Twilight to Highlight: The Physics of Supernovae*, ed. W. Hillebrandt & B. Leibundgut (Berlin: Springer), 97
- MacFadyen, A. I., & Woosley, S. E. 1999, *ApJ*, 524, 262
- MacFadyen, A. I., Woosley, W. E., & Heger, A. 2001, *ApJ*, 550, 410
- Maeda, K. 2004, Ph.D thesis, Univ. Tokyo
- Maeda, K., Nakamura, T., Nomoto, K., Mazzali, P. A., Patat, F., & Hachisu, I. 2002, *ApJ*, 565, 405
- Maeda, K., & Nomoto, K. 2003, *ApJ*, 598, 1163
- Maeda, K., Nomoto, K., Mazzali, P. A., & Deng, J. 2006, *ApJ*, 640, 854
- Maeder, A., & Meynet, G. 2004, *A&A*, 422, 225
- Marchant, A. B., & Shapiro, S. L. 1980, *ApJ*, 239, 685
- Matsumoto, H., Tsuru, T. G., Koyama, K., Awaki, K., Canizares, C. R., Kawai, N., Matsushita, S., & Kawabe, R. 2001, *ApJ*, 547, L25
- Matteucci, F., & Calura, F. 2005, *MNRAS*, 360, 447
- Nagataki, S. 2000, *ApJS*, 127, 141
- Nakamura, F., & Umemura, M. 1999, *ApJ*, 515, 239
- Nakamura, T., Umeda, H., Iwamoto, K., Nomoto, K., Hashimoto, M., Hix, W. R., & Thielemann, F.-K. 2001, *ApJ*, 555, 880
- Narayan, R., Piran, T., & Kumer, P. 2001, *ApJ*, 557, 949
- Nomoto, K., & Hashimoto, M. 1988, *Phys. Rep.*, 163, 13
- Nomoto, K., Maeda, K., Umeda, H., Ohkubo, T., Deng, J., & Mazzali, P. 2003, in *IAU Symp. 212, A Massive Star Odyssey*, ed. V. D. Hucht, A. Herrero, & C. Esteban (San Francisco: ASP), 395
- Oh, S. P., & Haiman, Z. 2002, *ApJ*, 569, 558
- Omukai, K., & Palla, F. 2003, *ApJ*, 589, 677
- Origlia, L., Ranalli, P., Comastri, A., & Maiolino, R. 2004, *ApJ*, 606, 862
- Peterson, J. R., et al. 2003, *ApJ*, 590, 207
- Portegies Zwart, S. F. 2006, in *Joint Evolution of Black Holes and Galaxies*, ed. M. Colpi, F. Haardt, & U. Moschella (Bristol: IOP), 387
- Portegies Zwart, S. F., Baumgardt, H., Hut, P., Makino, J., & McMillan, S. L. W. 2004, *Nature*, 428, 724
- Portegies Zwart, S. F., Makino, J., McMillan, S. L. W., & Hut, P. 1999, *A&A*, 348, 117
- Pruet, J., Surman, R., & McLaughlin, G. C. 2004, *ApJ*, 602, L101
- Qian, Y.-Z., Sargent, W. L. W., & Wasserburg, G. J. 2002, *ApJ*, 569, L61
- Qian, Y.-Z., & Wasserburg, G. J. 2002, *ApJ*, 567, 515
- Rakavy, G., Shaviv, G., & Zinamon, Z. 1967, *ApJ*, 150, 131
- Ranalli, P., Origlia, A., Comastri, A., Maiolino, R., & Makishima, K. 2005, preprint (astro-ph/0511021)
- Rees, M. J. 2002, in *Lighthouses of the Universe*, ed. M. Gilfanov, R. Sunyaev, & E. Churazov (Berlin: Springer), 345
- . 2003, in *The Future of Theoretical Physics and Cosmology*, ed. G. W. Gibbons, E. P. S. Shellard, & S. J. Rankin (Cambridge: Cambridge Univ. Press), 217
- Schaerer, D. 2002, *A&A*, 382, 28
- Schaye, J., Aguirre, A., Kim, T.-S., Theuns, T., Rauch, M., & Sargent, W. L. W. 2003, *ApJ*, 596, 768
- Shibata, M., & Shapiro, S. L. 2002, *ApJ*, 572, L39
- Somerville, R. S., Bullock, J. S., & Livio, M. 2003, *ApJ*, 593, 616
- Songaila, A. 2001, *ApJ*, 561, L153
- Songaila, A., & Cowie, L. L. 1996, *AJ*, 112, 335
- Stringfellow, G. S., & Woosley, S. E. 1988, in *The Origin and Distribution of the Elements*, ed. G. J. Mathews (Singapore: World Scientific), 467
- Tan, J. C., & McKee, C. F. 2004, *ApJ*, 603, 383
- Thielemann, F.-K., Nomoto, K., & Hashimoto, M. 1996, *ApJ*, 460, 408
- Tsuru, T. G., Awaki, H., Koyama, K., & Ptak, A. 1997, *PASJ*, 49, 619
- Tumlinson, J., & Shull, J. H. 2000, *ApJ*, 528, L65
- Tumlinson, J., Venkatesan, A., & Shull, J. M. 2004, *ApJ*, 612, 602
- Umeda, H., & Nomoto, K. 2002, *ApJ*, 565, 385
- . 2003, *Nature*, 422, 871
- Umeda, H., Nomoto, K., & Nakamura, T. 2000, in *The First Stars*, ed. A. Weiss et al. (Berlin: Springer), 150
- Umeda, H., Nomoto, K., Tsuru, T. G., & Matsumoto, H. 2002, *ApJ*, 578, 855
- Venkatesan, A., & Truran, J. W. 2003, *ApJ*, 594, L1
- Venkatesan, A., Tumlinson, J., & Shull, J. M. 2003, *ApJ*, 584, 621
- Wasserburg, G. J., & Qian, Y.-Z. 2000, *ApJ*, 529, L21
- Woosley, S. E. 1986, in *Nucleosynthesis and Chemical Evolution*, ed. B. Hauck, A. Maeder, & G. Meynet (Switzerland: Geneva Obs.), 1
- Yoshida, N., Bromm, B., & Hernquist, L. 2004, *ApJ*, 605, 579